Monthly Notices of the ROYAL ASTRONOMICAL SOCIETY

MNRAS **531,** 4692–4713 (2024) https://doi.org/10.1093/mnras/stae1456
Advance Access publication 2024 June 12

Unveiling the 3D structure of magnetosheath jets

S. Fatemi,[1]★ M. Hamrin,[1] E. Krämer,[1] H. Gunell,[1] G. Nordin,[1] T. Karlsson[2] and O. Goncharov[3]

[1]*Department of Physics, Umeå University, SE-90187 Umeå, Sweden*
[2]*School of Electric Engineering and Computer Science, KTH Royal Institute of Technology, SE-100 44, Stockholm Sweden*
[3]*Faculty of Mathematics and Physics, Charles University, 121 16, Prague, The Czech Republic*

Accepted 2024 June 4. Received 2024 June 1; in original form 2024 April 17

ABSTRACT

Magnetosheath jets represent localized enhancements in dynamic pressure observed within the magnetosheath. These energetic entities, carrying excess energy and momentum, can impact the magnetopause and disrupt the magnetosphere. Therefore, they play a vital role in coupling the solar wind and terrestrial magnetosphere. However, our understanding of the morphology and formation of these complex, transient events remains incomplete over two decades after their initial observation. Previous studies have relied on oversimplified assumptions, considering jets as elongated cylinders with dimensions ranging from 0.1 R_E to 5 R_E (Earth radii). In this study, we present simulation results obtained from Amitis, a high-performance hybrid-kinetic plasma framework (particle ions and fluid electrons) running in parallel on graphics processing units (GPUs) for fast and more environmentally friendly computation compared to CPU-based models. Considering realistic scales, we present the first global, three-dimensional (3D in both configuration and velocity spaces) hybrid-kinetic simulation results of the interaction between solar wind plasma and the Earth. Our high-resolution kinetic simulations reveal the 3D structure of magnetosheath jets, showing that jets are far from being simple cylinders. Instead, they exhibit intricate and highly interconnected structures with dynamic 3D characteristics. As they move through the magnetosheath, they wrinkle, fold, merge, and split in complex ways before a subset reaches the magnetopause.

Key words: planet-stars interactionlanet–star interactionspla s – methods: numerical – planets and satellites: terrestrial planets – planets and satellites: magnetic fields – plasmas.

1 INTRODUCTION

The magnetosheath is a region confined between the planetary bow shock (a boundary where the supersonic flow of the solar wind is decelerated, deflected, and heated) and the magnetopause (the outermost boundary of the magnetosphere). In this highly dynamic region, the properties of the solar wind plasma and magnetic field undergo significant changes due to compression and turbulence, making the magnetosheath a crucial region for understanding the interaction between the solar wind and planetary magnetosphere (recently reviewed by Narita, Plaschke & Vörös 2021).

In the last two decades, spacecraft observations have frequently reported localized and temporary enhancements of plasma dynamic pressure in the magnetosheath of the Earth, characterized by a sudden increase in plasma velocity and/or density compared to the surrounding magnetosheath plasma (Němeček et al. 1998; Savin et al. 2008; Hietala et al. 2009; Karlsson et al. 2012; Archer & Horbury 2013; Hietala & Plaschke 2013; Plaschke, Hietala & Angelopoulos 2013; Gunell et al. 2014; Gutynska, Sibeck & Omidi 2015; Plaschke et al. 2017; Goncharov et al. 2020; Plaschke, Hietala & Vörös 2020; Raptis et al. 2020). These enhancements have been observed more often at the subsolar magnetosheath downstream of a quasi-parallel shock, i.e. when the interplanetary magnetic field (IMF) has a small cone angle ($<30^\circ$ with respect to the Earth–Sun line) (Archer & Horbury 2013; Plaschke et al. 2013; Vuorinen, Hietala & Plaschke 2019; LaMoury et al. 2021). Similar phenomena have recently been observed in the magnetosheath of Mars (Gunell et al. 2023) and Jupiter (Zhou et al. 2024).

Currently, there is no general consensus on the nomenclature of these dynamic pressure enhancements, indicating a lack of comprehension of their underlying nature and characteristics. Throughout the years, various terminologies have been employed to describe these phenomena including 'transient flux enhancements' (Němeček et al. 1998), 'fast plasma streams' (Savin et al. 2012), 'high-energy density jets' (Savin et al. 2008), 'plasmoids' (Karlsson et al. 2012; Gunell et al. 2014; Karlsson et al. 2015), 'high-speed jets' (Plaschke et al. 2013, 2017), and 'magnetosheath jets' (Hietala et al. 2012; Dmitriev & Suvorova 2015). We adopt the term 'jets' in this study.

Previous analyses of the observed magnetosheath jets have provided different results regarding the morphology of the jets, particularly their sizes and structures (Plaschke et al. 2018). The early event studies indicated that the typical size of jets in the direction parallel to their flow motion is around 1 R_E (Archer, Horbury & Eastwood 2012), where $R_E = 6371$ km is the mean radius of the Earth. However, large flow-parallel scale sizes (5 R_E) have also been observed (Dmitriev & Suvorova 2012). Similarly, there is a wide spread in the flow-perpendicular dimension of jets, ranging

★ E-mail: shahab.fatemi@amitiscode.com; shahab.fatemi@umu.se

from 0.2 R_E to a few R_E (Archer et al. 2012; Hietala et al. 2012; Gunell et al. 2014). Later, statistical analyses estimated 0.7 R_E for the flow-parallel dimension and nearly twice as large for the flow-perpendicular dimension of the jets (Plaschke et al. 2013). Recent re-analysis of jets suggested that the scales of jets follow a lognormal distribution (Plaschke et al. 2020). This has led to a significant reduction in their estimated sizes, with median scales of $0.15R_E$ and $0.12R_E$ for the flow-parallel and flow-perpendicular dimensions, respectively (Plaschke et al. 2020). Despite substantial adjustments in the estimation of jet sizes, the earlier findings concerning the rate of large jets ($>1R_E$) impacting the magnetopause (3 per hour, in general) remained unchanged (Plaschke et al. 2020).

In addition to observations, both local- and global-scale kinetic simulations of the Earth's magnetosheath have investigated the properties and scales of jets, and they have greatly advanced our understanding of these mysterious phenomena (Gutynska et al. 2015; Omidi et al. 2016; Hao et al. 2016a; Palmroth et al. 2018; Voitcu & Echim 2018; Preisser et al. 2020; Omelchenko, Chen & Ng 2021; Palmroth et al. 2021; Suni et al. 2021; Guo et al. 2022). These simulations, similar to observations, revealed a broad range of sizes for jets from $0.2R_E$ to a few R_E at various directions. None the less, they consistently demonstrated that the size of jets is larger in flow-parallel compared to flow-perpendicular directions (e.g. Hao et al. 2016a; Palmroth et al. 2018, 2021; Guo et al. 2022).

The uncertainties encountered in understanding the structure of these jets can be associated with oversimplified assumptions employed in their analyses. These assumptions often portray jets as either cylinder-, pancake-, or finger-like shapes, exhibiting diverse sizes aligned in parallel or perpendicular directions to the plasma flow or magnetic field orientation (Archer et al. 2012; Karlsson et al. 2012; Plaschke et al. 2016, 2018; Goncharov et al. 2020; Plaschke et al. 2020; Palmroth et al. 2021; Guo et al. 2022). In addition, all the previously applied kinetic models to investigate magnetosheath jets have either been two-dimensional (2D) models in the spatial domain (configuration space) (Gutynska et al. 2015; Omidi et al. 2016; Hao et al. 2016a; Palmroth et al. 2018; Preisser et al. 2020; Palmroth et al. 2021; Suni et al. 2021; Guo et al. 2022) or three-dimensional (3D) models with reduced scales of the Earth (Karimabadi et al. 2014; Omidi et al. 2016; Ng, Chen & Omelchenko 2021; Omelchenko et al. 2021) or focused on a small region in the magnetosheath (e.g. Voitcu & Echim 2018). Furthermore, spacecraft observations at specific locations in the magnetosheath are unable to cover and probe a large spatial area at once and therefore provide a limited '1D snapshot' view of jets. Consequently, due to the lack of comprehension of the structure of the jets, several assumptions and simplifications have been made that can lead to uncertainties and ambiguities in our understanding of the morphology of these phenomena.

In addition to their sizes and structures, the formation mechanism of jets has also remained elusive (Plaschke et al. 2018, 2020). Observations suggest that the occurrence of jets downstream of the quasi-parallel shock is more frequent in proximity to the bow shock as compared to the magnetopause (Archer & Horbury 2013; Plaschke et al. 2013; Goncharov et al. 2020). On the contrary, the occurrence frequency of jets increases towards the magnetopause downstream of the quasi-perpendicular shock (Archer & Horbury 2013). It has been suggested that the formation of jets downstream of the quasi-parallel shock can be linked to the foreshock structures and/or the bow shock ripples, and reformation (Hietala & Plaschke 2013; Gutynska et al. 2015; Karlsson et al. 2015; Omidi et al. 2016; Hao et al. 2016a, b; Kajdič et al. 2017; Suni et al. 2021; Raptis et al. 2022a). Moreover, jets have been observed more frequently when the IMF exhibits a higher level of stability (Savin et al. 2008; Hietala et al. 2009; Archer & Horbury 2013; Plaschke et al. 2013). This suggests that, in general, the formation of jets is not directly associated with IMF discontinuities or transient events such as magnetic discontinuities and hot flow anomalies (Hietala & Plaschke 2013; Plaschke et al. 2013; Karimabadi et al. 2014; Suni et al. 2021; Raptis et al. 2022a).

Despite the lack of understanding of the nature and formation mechanism of magnetosheath jets, observations have found compelling evidence that jets play a crucial role in coupling between the solar wind and planetary magnetospheres by transferring a significant amount of energy and momentum towards and into the magnetosphere (Savin et al. 2008; Shue et al. 2009; Gunell et al. 2012; Savin et al. 2012; Gunell et al. 2014; Dmitriev & Suvorova 2015; Plaschke et al. 2016). They also contribute to various fundamental plasma processes, such as wave generation (Karlsson et al. 2018; Wang et al. 2022; Krämer et al. 2023), plasma acceleration (Lavraud et al. 2007; Liu et al. 2019), and magnetic reconnection (Phan et al. 2007; Hietala et al. 2018; Ng et al. 2021). Beyond their impact on the magnetosphere, these jets exhibit observable effects even on the ground, including geomagnetic disturbances, enhancements in ionospheric outflow, and dayside aurora (Hietala et al. 2012; Han et al. 2016; Wang et al. 2018; Norenius et al. 2021; Wang et al. 2022). Such far-reaching influences highlight the significance of the jets in the solar wind coupling with the magnetosphere and ionosphere of the Earth (Plaschke et al. 2018; Rakhmanova et al. 2023). However, the extent of their impact remains uncertain, mainly due to our limited understanding of their structure, dimensions, and formation mechanisms (Plaschke et al. 2018).

In this study, we present the first 3D configuration of magnetosheath jets using the Amitis code, a state-of-the-art hybrid-kinetic plasma model (Fatemi et al. 2017). We have successfully resolved, for the first time, the time-dependent, global 3D interaction (both spatial and velocity domains) between the solar wind and the Earth's magnetosphere. By simulating typical solar wind conditions near the orbit of the Earth, we present a new view of the structure of jets forming within the magnetosheath.

2 MODEL AND METHODS

2.1 Amitis model

In this study, we use an upgraded version of the Amitis code, a high-performance hybrid-kinetic plasma model that runs in parallel on multiple graphics processing units (GPUs) instead of a single GPU (Fatemi et al. 2017, 2022). Amitis is 3D in both configuration and velocity spaces, time-dependent, and grid-based kinetic plasma frameworks (Fatemi et al. 2017). In this model, the ions are kinetic, charged macro-particles, and electrons are a massless, charge-neutralizing fluid. The model is the first of its kind that runs entirely on GPUs, and it runs at least 10 times faster and more energy and cost-efficient (environmentally friendly) compared to its parallel CPU-based predecessors (Fatemi et al. 2017).

In our model, an ion position, $\boldsymbol{r}_i$, and velocity, $\boldsymbol{v}_i$, are obtained from the Lorentz equation of motion

$$\frac{\mathrm{d}\boldsymbol{v}_i}{\mathrm{d}t} = \frac{q_i}{m_i}\left(\boldsymbol{E} + \boldsymbol{v}_i \times \boldsymbol{B}\right), \qquad \frac{\mathrm{d}\boldsymbol{r}_i}{\mathrm{d}t} = \boldsymbol{v}_i, \tag{1}$$

where q_i and m_i are the charge and mass of a macro-particle ion, respectively. $\boldsymbol{E}$ is the electric field and $\boldsymbol{B}$ is the magnetic field applied to the ion at its position. We calculate the electric field from the electron momentum equation for mass-less electrons ($m_e = 0$), which

is given by

$$\boldsymbol{E} = \overbrace{\boldsymbol{J} \times \boldsymbol{B}/\rho_i}^{\text{Hall}} + \overbrace{\eta \boldsymbol{J}}^{\text{Ohmic}} - \overbrace{\boldsymbol{u}_i \times \boldsymbol{B}}^{\text{Convective}} - \overbrace{\nabla p_e/\rho_i}^{\text{Ambipolar}}, \quad (2)$$

where $\boldsymbol{J}$ is the electric current density calculated from Ampère's law where displacement current is neglected (i.e. $\boldsymbol{J} = \nabla \times \boldsymbol{B}/\mu_0$), ρ_i is the charge density of macro-particle ions, η is the resistivity, $\boldsymbol{u}_i$ is the bulk flow velocity of ions, and p_e is the electron pressure. Different electric field terms including the Hall, ohmic, convective, and ambipolar electric fields are labelled in equation (2). Amitis can solve electron pressure tensors, but for simplicity in this study, we assume that electrons are an ideal gas with $p_e \propto n_i^{\gamma}$, where $\gamma = 5/3$ is the adiabatic index and n_i is the ion density (e.g. Holmström et al. 2012; Fatemi et al. 2013). Therefore, the pressure gradient in equation (2) is comparable to the ion density gradient in our model. We advance the magnetic field in time using Faraday's law, $\partial \boldsymbol{B}/\partial t = -\nabla \times \boldsymbol{E}$. The model principles are described in detail by Fatemi et al. (2017).

Amitis has been extensively applied to study plasma interactions with various planetary bodies, including the Moon, Mercury, Ganymede, Mars, comets, and several asteroids (e.g. Fatemi et al. 2017; Fuqua-Haviland et al. 2019; Fatemi, Poppe & Barabash 2020; Aizawa et al. 2021; Poppe, Garrick-Bethell & Fatemi 2021; Fatemi et al. 2022; Rasca, Fatemi & Farrell 2022; Shi et al. 2022; Poppe & Fatemi 2023; Wang et al. 2023; Gunell, Goetz & Fatemi 2024). In addition, its results have been successfully validated through comparison with spacecraft observations (e.g. Fatemi et al. 2017, 2020; Aizawa et al. 2021; Fatemi et al. 2022; Rasca et al. 2022; Wang et al. 2023), theories (Fuqua-Haviland et al. 2019), and other hybrid-kinetic and magnetohydrodynamic (MHD) models (Fatemi et al. 2017; Aizawa et al. 2021).

2.2 Coordinate system and simulation set-up

In our analysis, we utilize the Geocentric Solar Magnetospheric (GSM) coordinate system, which is centred at the Earth's centre of mass. In this coordinate system, the $+x$-axis is directed towards the Sun, representing the direction opposite to the flow direction of the solar wind. The $+z$-axis points to the northern magnetic pole and the $+y$-axis completes the right-handed coordinate system. To perform our simulations, we employ a simulation domain with dimensions $-19\ R_E \leq x \leq +53\ R_E$ and at smallest $-55\ R_E \leq (y, z) \leq +55\ R_E$, where $1R_E = 6371$ km is the radius of the Earth in our simulations. To discretize our simulation domain, we employ a regularly spaced Cartesian grid with cubic cells of size 500 km ($\approx$0.078 R_E).

The focus of this study is on the structure of the solar wind interaction with the dayside magnetosphere, primarily the magnetosheath jets. Therefore, we exclude the simulation of the Earth's atmosphere, ionosphere, and exosphere by assuming that the inner boundary of the magnetosphere is a conductive sphere with a radius of 30 000 km ($\approx$4.7 R_E), centred at the origin of our coordinate system. When a particle impacts this inner boundary, we remove that particle from the simulation domain. The choice for the size and configuration of the inner boundary aligns with previous simulations of the Earth by the Vlasiator model (e.g. Palmroth et al. 2018, 2021).

The inflow boundary ($x = +53\ R_E$) and the outflow boundary ($x = -19\ R_E$) of our simulations act as a perfect plasma absorber. At the inflow boundary, kinetic macro-particles are continuously injected into the simulation domain, following a drifting Maxwellian velocity distribution function. Along the y- and z-axes, the boundaries are assumed to be periodic for both electromagnetic fields and particles. This means that along the y- and z-axes, the electromagnetic fields and particles are replicated from one side to the other side of the simulation domain.

We incorporate the actual scales of the Earth's magnetic field in our simulations. We adopt a magnetic dipole model with a magnetic moment $M = 8.22 \times 10^{22}$ A m^2 (Walt 1994) positioned at the centre of the Earth and oriented exactly along the $-z$-axis. This magnetic moment generates a surface equatorial magnetic field of $\sim$32 μT at a distance of 1 R_E, and $\sim$305 nT at the inner boundary (plasma absorber) of our simulations at 4.7 R_E.

At the inflow boundary where the solar wind enters our simulation domain, we employ 32 macro-particles per grid cell consisting exclusively of protons with mass 1.67×10^{-27} kg and charge 1.60×10^{-19} C. For simplicity, we do not include solar wind He^{++} or heavier ions (e.g. O^{+6}) in our simulations, explained in detail in Section 2.5. Within our simulation domain, we track the trajectories of over 40 billion macro-particle protons at every simulation time-step. To achieve this, we utilize a time-step of $\Delta t = 8 \times 10^{-3}$ s, which is 5×10^{-4} of the upstream solar wind proton gyro-period away from magnetospheric disturbances and is 3×10^{-2} of a proton gyro-period near magnetospheric poles at the inner boundary of our simulations. By employing such a small time-step, we ensure that the gyromotion of the solar wind protons is fully resolved within the entire simulation domain and Courant–Friedrich–Lewy (CFL) condition is fulfilled.

Within our model, the plasma resistivity is uniformly set to 10^4 Ω m wherever the ions exist. This resistivity is primarily required to damp numerical oscillations and to facilitate magnetic reconnection to occur in our simulations (Fatemi et al. 2017, 2020, 2022). To effectively handle the vacuum regions that arise in our simulations, such as those found in the magnetotail, we incorporate a vacuum resistivity of 0.2×10^7 Ω m, as described in Holmström (2013) and Fatemi et al. (2017). Whenever the density of a grid cell falls below 1 per cent of the undisturbed (upstream) solar wind plasma density, we dynamically assign the vacuum resistivity to those cells. In these vacuum regions, we solve the magnetic diffusion equation instead of utilizing general Faraday's law, as explained in detail by Holmström (2013) and Fatemi et al. (2017).

In this study, we perform a series of hybrid simulations using the Amitis code for the 'typical' solar wind conditions near the Earth, i.e. the solar wind speed of 400 km s^{-1}, plasma density of 7 cm^{-1}, and magnetic field strength of 5 nT (Kivelson & Russell 1995). The solar wind plasma and magnetic field configurations applied in our simulations are summarized in Table 1. In this table, the calculation for plasma dynamic pressure, represented as P_{dyn}, is given by $P_{dyn} = mn\boldsymbol{v}^2$, where m represents the proton mass, n is the plasma density, and $\boldsymbol{v}$ is the plasma flow velocity. In the solar wind, $P_{sw} = mn_{sw}v_{sw}^2$. The plasma β denotes the ratio between the solar wind thermal pressure and the magnetic pressure. M_A, M_s, and M_{ms} are the Alfvén, sonic, and magnetosonic Mach numbers, respectively.

Our simulations consisted of different scenarios. First, we conducted a simulation where the IMF is directed radially outward from the Sun (run R1), forming a 15° angle from the solar wind flow direction (i.e. quasi-parallel to the solar wind flow). Note that in this manuscript, the term 'quasi-parallel IMF' refers to the direction of the IMF relative to the upstream solar wind flow direction, and not to the bow shock normal, unless stated otherwise. As outlined in Table 1, the R1 simulation run consists of three distinct IMF configurations. Initially, the IMF had only x and y components (run R1Y). After approximately 11 min of physical time, we changed the IMF orientation upstream in our simulations (i.e. the inflow boundary) and made it southward (R1S), propagating into the simulation domain while the magnitude and cone angle of the IMF

Table 1. Solar wind plasma parameters and IMF configurations applied in our simulations. All the plasma parameters listed in columns 3 to 11 are the same between the simulation runs. Only the IMF orientation is different between the runs.

Run	$\boldsymbol{B}_{\rm IMF}(B_x, B_y, B_z)$ (nT)	$\boldsymbol{B}$ (nT)	$n_{\rm sw}$ ($\rm cm^{-3}$)	$\boldsymbol{v}_{\rm sw}(v_x, v_y, v_z)$ ($\rm km\,s^{-1}$)	$T_{\rm i} = T_{\rm e}$ (eV)	$P_{\rm sw}$ (nPa)	β	$M_{\rm A}$	$M_{\rm s}$	$M_{\rm ms}$
R1Y	(+4.83, −1.30, 0.0)	5.0	7.0	(−400, 0, 0)	10.0	1.86	1.1	9.7	7.1	5.7
R1S	(+4.83, 0.0, −1.30)	–	–	–	–	–	–	–	–	–
R1N	(+4.83, 0.0, +1.30)	–	–	–	–	–	–	–	–	–
R2	(0.0, +5.0, 0.0)	–	–	–	–	–	–	–	–	–

remained unchanged. Subsequently, after nearly 35 min, we again changed the IMF to a northward orientation (R1N). This allowed us to simulate the passage of two consecutive current sheets (magnetic transients) through our simulations.

In the R1 simulation, the IMF changes occurred in the format of a step-function where the magnetic field orientation changed. For example, see time 12:30 in Fig. B8(d) in Appendix B, where the y-component of the magnetic field changes from +1.3 nT to zero, and the z-component of the magnetic field changes from zero to −1.3 nT. However, due to the non-zero plasma resistivity applied in our simulations ($10^4\ \Omega$ m), these changes formed a magnetic transient (current sheet) with a width of $\approx 1\ R_E$ propagating through the entire simulation domain, interacting with the Earth. Choosing a smaller plasma resistivity results in a narrower current sheet but increases the numerical noise in our simulations. Before the arrival of the current sheet and after its passage, the solar wind parameters and magnetic field configurations remained constant upstream of our simulation domain, indicating a relatively constant environment in terms of solar wind conditions and magnetic field configurations.

In addition to the R1 simulation series, we conducted one simulation with the IMF perpendicular to the solar wind flow direction (R2), listed in Table 1. Throughout this run, we maintained a fixed IMF orientation without making any changes. The solar wind plasma parameters including plasma density, velocity, and temperature remained unchanged during both R1 and R2 simulations.

The simulation results presented here (Figs 1–7) are taken before the arrival of the current sheets at $x = +25\ R_{\rm E}$ and/or long after the previous current sheet passed the dayside magnetosphere. This ensures that the dayside magnetosphere has responded to the magnetic transients and fully developed, and is stable in the analyses presented in this manuscript. Detailed investigations on the response of the magnetosphere to magnetic transients and how the bow shock, magnetosheath jets, and magnetopause respond to IMF variations are beyond the scope of this study, saved for future research.

2.3 Jet selection criteria

Various methods have been applied to detect magnetosheath jets from observed spacecraft data, summarized in Plaschke et al. (2018). Among those, two general approaches are commonly used: (a) comparing observed features with time-averaged local background conditions in the magnetosheath (Karlsson et al. 2012; Archer & Horbury 2013), and (b) comparing the observed features with undisturbed solar wind plasma and magnetic field upstream of the bow shock (Plaschke et al. 2013). However, both methods have limitations, as thoroughly reviewed by Plaschke et al. (2018). Utilizing a running average (often tens of minutes) to establish the local background imposes a limitation on the time-scales of detectable transient events, like jets (Plaschke et al. 2013). The averaging time-scales must be considerably longer than the duration of most transients and exceed their typical recurrence time-scale (Archer & Horbury 2013; Plaschke et al. 2013). Comparison with the upstream solar wind conditions allows for a broader range of time-scales, but it requires information on the solar wind, which is often not readily available to a spacecraft located downstream of the bow shock. Therefore, the solar wind observations by other satellites that continuously monitor the solar wind plasmas are used (e.g. ACE or WIND spacecraft data) and time-shifted to the nominal subsolar bow shock (e.g. Plaschke et al. 2013, 2018). This time-shifting method can introduce complications and uncertainties in analysing the data in the magnetosheath and the magnetosphere of the Earth. However, this is not an issue in numerical simulations, because the upstream conditions are very well known and can be accurately tracked in time in the simulations. Therefore, we use the latter approach in this study (i.e. method b).

One of the commonly employed thresholds using upstream solar wind conditions is $P_{{\rm dyn},x} \geq 0.5 P_{\rm sw}$, where $P_{{\rm dyn},x}$ is the dynamic pressure in the magnetosheath along the x-axis, and $P_{\rm sw}$ is the solar wind dynamic pressure, explained by Plaschke et al. (2013). This threshold, referred to as the 'Plaschke criterion' throughout this study, should only be applied to the subsolar region (Plaschke et al. 2013). We use this criterion to select jets in the magnetosheath in our simulations. Since the IMF is nearly parallel to the solar wind flow direction during the R1 simulation run, and our focus is on the magnetosheath jets forming near the subsolar region, the Plaschke criterion is a valid assumption in the analyses presented in this study. We limit our investigations spatially to the subsolar region with a maximum 30° deviation from the Earth–Sun line (Plaschke et al. 2013, 2018).

2.4 Magnetospheric boundary selection criteria

Determining magnetospheric boundaries, such as the bow shock and the magnetopause, in the subsolar region during quasi-parallel IMF configurations is not straightforward due to the disturbances associated with the foreshock. This complication holds for both simulations and spacecraft data. Our approach to select these boundaries in our simulations primarily relies on analysing the intensity and direction of electric currents, $\boldsymbol{J}$, computed from Ampère's law using our simulation data, a privilege available for 3D simulations. In previous studies, we successfully employed this method to identify magnetospheric boundaries at Mercury (Fatemi et al. 2018, 2020) and Ganymede (Fatemi et al. 2022). While the electric current density is our primary method to identify magnetospheric boundaries for the R1 simulation series; however, the presence of the foreshock region makes it challenging to accurately pinpoint the bow shock's location in the subsolar region. To address this issue, we incorporate additional criteria in conjunction with the electric current density analysis. The criteria are as follows:

(i) The electric current intensity should exceed $3\,n\rm A/m^2$ at the boundary,

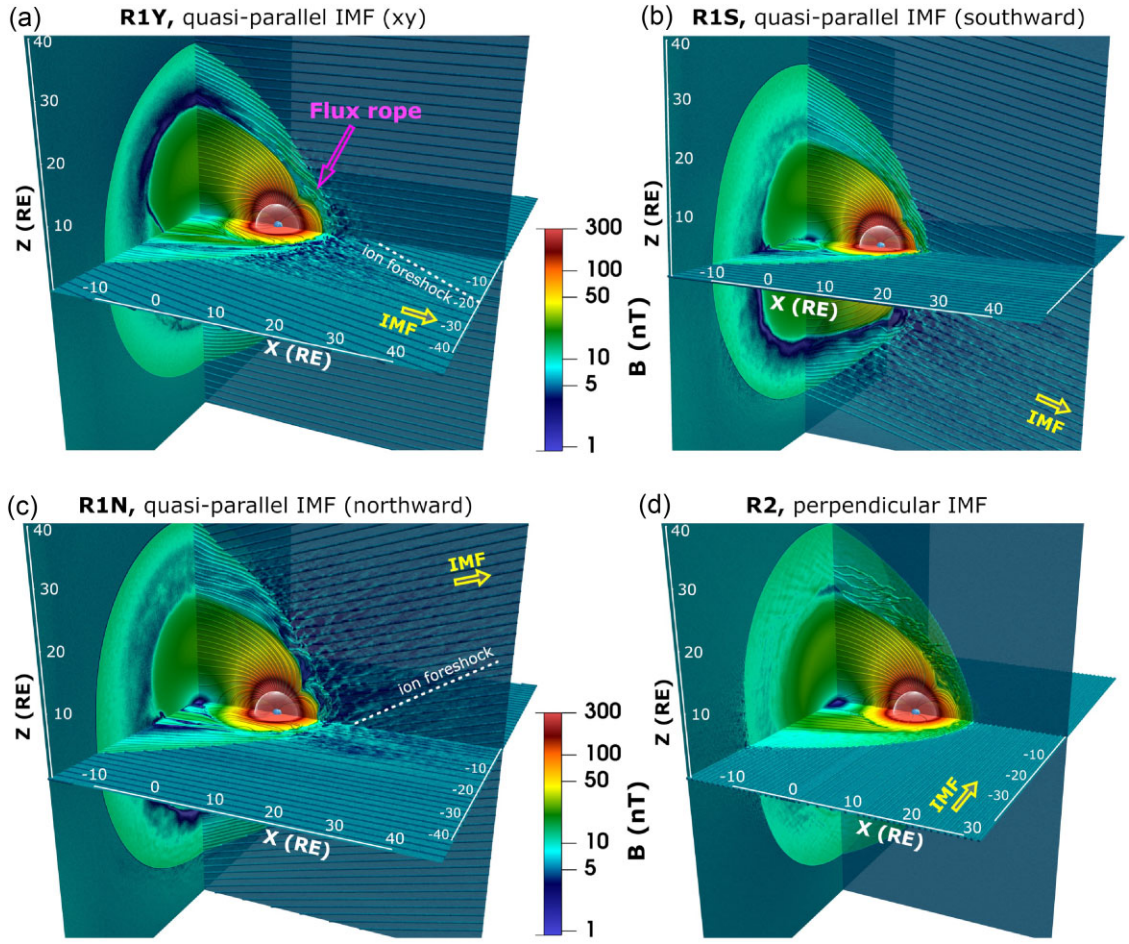

Figure 1. Time snapshot of the global, high-resolution, 3D structure of the solar wind interaction with the Earth obtained from the Amitis hybrid model. The results are presented in the GSM coordinate system for (a) a quasi-parallel IMF to the solar wind flow direction without any B_z component, i.e. run R1Y, (b) a quasi-parallel IMF with a southward component, i.e. run R1S, (c) a quasi-parallel IMF with a northward component, i.e. run R1N, and (d) a perpendicular IMF where only the B_y is non-zero, i.e. run R2. Note that the term 'quasi-parallel' here refers to the orientation of the IMF with respect to the upstream solar wind plasma flow direction. The solar wind flows along the $-x$-axis. All simulation parameters are summarized in Table 1 and explained in Section 2. The background colour shows the magnitude of the magnetic field in logarithmic scale in the xy (equatorial) plane at $z = 0$, the xz (mid-night meridian) plane at $y = 0$, and the yz plane at $x \approx -18.5\ R_E$ in all panels. Streamlines shown in a few planes are magnetic field line tracing at that corresponding plane. For visualization purposes of the streamlines, we set the third component of the magnetic field to zero. The yellow arrows show the IMF orientation at each panel. The pink arrow in Fig. 1(a) points to a flux rope in the magnetosheath over the northern cusp. The Earth is shown by a small blue sphere, centred at the origin of the coordinate system, surrounded by a transparent sphere of radius $4.7\,R_E$, indicating the inner boundary of our simulations. The dashed white lines in Figs 1(a) and (c) are parallel to the ion foreshock boundaries, shown to guide the eyes, indicating the ion foreshock boundary is not aligned with the IMF. See Movies A4 and A5 in Appendix A for the time evolution of the magnetosphere during the R1Y and R1S simulations.

(ii) The plasma density downstream of the bow shock boundary should be higher than the upstream solar wind plasma density due to solar wind compression at the bow shock, and

(iii) The bulk flow speed downstream of the bow shock boundary should be smaller than the solar wind plasma speed due to the deceleration of plasma at the bow shock.

To identify the magnetopause boundary, we use the electric current density, and we choose $9\,nA/m^2$ as the minimum requirement for the current density at the magnetopause. Using these criteria, we selected the magnetopause and bow shock boundaries in our simulations. To validate our simulation results, we compare the location of the bow shock and magnetopause boundaries obtained from our simulations with an empirical model by Chao et al. (2002).

2.5 Limitations in simulations

The presented results in this study come with certain limitations primarily due to the applied numerical method and the limited computational resources. The main limitations of this study are as follows:

(i) In our simulations, we focus exclusively on the solar wind protons and their impact on the overall interaction between the solar wind and the Earth. Notably, the solar wind is comprised of various multiply charged heavy ion species like He^{+2}, O^{+6}, Si^{+8}, and Fe^{+9} (Bame et al. 1970; Bochsler 2007). However, protons are the dominant solar wind ion species (averaging over 95 per cent), and for simplicity, we do not include heavy ions in this study. While the current version of Amitis is capable of handling over 10 ion species (e.g. Poppe et al. 2021), investigating the effect of the heavy ions in

the formation, evolution, and morphology of the jets is an interesting research topic that remains for future investigation.

(ii) The nature of hybrid models prevents us from including electron dynamics and their contributions to the interaction with the magnetosphere in this study. In addition, due to the lack of electron dynamics, our simulations underestimate the plasma acceleration associated with charge separation. As previously discussed by Fatemi, Holmström & Futaana (2012), the ambipolar electric field in hybrid models, which is related to the electron pressure gradient shown in equation (2), typically contributes less to plasma energization compared to simulations that explicitly resolve electron dynamics. Currently, the space physics community lacks a fully kinetic plasma model that accurately handles electron dynamics and includes 3D plasma interaction with planetary bodies in their physical scales.

(iii) Generally, in a hybrid plasma model, the simulation cell size, ΔL, should be nearly an order of magnitude larger than δ_e, where $\delta_e = c/\omega_{pe}$ is the electron inertial length, c is the speed of light, and ω_{pe} is the electron plasma frequency (e.g. Harned (1982) and the review by Ledvina, Ma & Kallio (2008) and the references therein). For proton and electron, the ratio between the ion-inertial (δ_i) and electron-inertial length-scales $\delta_i/\delta_e = \sqrt{m_i/m_e} \approx 43$, where m_i and m_e are the proton and electron mass, respectively. Therefore, ΔL in a hybrid model should be larger than $10\delta_e/43 \approx 0.25\delta_i$. Although the simulation cell sizes in hybrid models are sometimes comparable to or smaller than the ion inertial length, Tóth et al. (2017) have shown that as long as the global scales of a simulation are larger than δ_i, the global solution is not sensitive to the actual value of δ_i. Their finding is in agreement with earlier hybrid simulations of various Solar system bodies obtained from different hybrid models where the simulation cell sizes are between $\sim 2\delta_i$ to $\sim 6\delta$i (e.g. Kallio 2005; Brain et al. 2010; Holmström et al. 2012; Müller et al. 2012; Fatemi et al. 2018; Exner et al. 2020; Jarvinen et al. 2020; Aizawa et al. 2021; Le et al. 2023), and sometimes even larger than $10\,\delta_i$ (e.g. Kallio & Janhunen 2004), chosen based on the kinetic scales of interest. However, some of the hybrid models that have chosen cell sizes comparable to or smaller than δ_i have scaled down the global physical size of the interaction region (e.g. Karimabadi et al. 2014; Herčík et al. 2016; Omelchenko et al. 2021), and therefore the relative size of δ_i to the interaction scale size is larger than the physical ratios. In all the simulation results presented here, we have used regular-spaced Cartesian cubic grids of size $\Delta L = 500$ km ($\approx 0.08\,R_E$), which is $\approx 5.8\,\delta_i$ for the solar wind parameters listed in Table 1. The global scales of the resolved phenomena in our simulations are larger than ΔL (e.g. the stand-off distance of the magnetopause is at $\approx 120\,\Delta L$), and the spatial length-scales of the magnetosheath jets are a few times, if not an order of magnitude, larger than ΔL. In addition, the local δ_i in the magnetosheath, where the jets appear, decreases to nearly half of that in the solar wind. Therefore, the selection for our cell sizes does not affect the global pattern of the jets and magnetospheric structures (e.g. foreshock, bow shock, and vortices) captured by the simulations presented in this study. However, it is worth noting that our presented results do not address jets of sizes smaller than ΔL.

(iv) Achieving extremely high simulation grid resolution (e.g. cell sizes comparable to or even smaller than δ_i) to simulate the global 3D kinetic structure of the Earth's magnetosphere using its physical scales, while desirable, has been a decadal challenge for computation and remains impossible using kinetic (particle-based) models even using cutting-edge technologies like GPUs, at least with the current size of GPU's internal memory (known as the global memory, which is maximum 80 GB on Nvidia A100 series at the time of this writing). Reducing the cell sizes from $5.8\delta_i$ to $1.0\delta_i$ requires using at least $5.8^3 \approx 200$ times more GPUs, which is currently not available to regular users of large-scale supercomputers. Quantum computing will perhaps help us to achieve extremely high-resolution simulations, but this capability is not fully developed yet and will be accessible in the future.

While our presented results in this study shed light on important aspects of magnetosheath jets and unveil their structure, it is important to acknowledge the limitations of our simulations when interpreting and generalizing the results. Future research with improved numerical methods and enhanced computational capabilities will help to address some of these constraints and provide a more comprehensive understanding of the subject matter.

3 RESULTS

Here, we present the first 3D simulation results of the structure of magnetosheath jets using physical scales of the Earth's magnetosphere. This detailed representation is obtained from the Amitis model, explained in Section 2. In our simulations, we use the typical solar wind plasma conditions near the Earth and a range of IMF orientations, outlined in Table 1. The spatial and temporal scales of the magnetosphere are represented in our model with no scaling being applied in our simulations.

3.1 Global 3D structure of the Earth's magnetosphere

First, we present the global, high-resolution, 3D kinetic interaction between the solar wind and the Earth for various IMF configurations, showing our model correctly captures the physics of the interaction. Fig. 1 presents a time-snapshot of the magnetic field obtained from our model for four distinct IMF configurations listed in Table 1: run R1Y for a quasi-parallel IMF to the solar wind flow without any B_z component (Fig. 1a), runs R1S and R1N for a quasi-parallel IMF to the solar wind flow with a southward and northward component, respectively (Figs 1(b) and (c)), and run R2 for a perpendicular IMF to the solar wind flow (Fig. 1d). Runs R1Y, R1S, and R1N are part of the same simulation sequence where the IMF orientation changes, as explained in Section 2. Note that the term 'quasi-parallel' here refers to the orientation of the IMF with respect to the upstream solar wind flow and not the bow shock normal.

In addition to the global structure of the magnetosphere, one notable characteristic observed in Figs 1(a)–(c) is the presence of a foreshock preceding the bow shock when the IMF is quasi-parallel to the solar wind (i.e. R1 simulation series). As marked in Figs 1(a) and (c), the ion foreshock does not align with the IMF and instead, it remains behind the tangent field line, which is consistent with foreshock ion observations (Russell & Hoppe 1983; Eastwood et al. 2005). However, when the IMF is perpendicular to the solar wind flow (Fig. 1d), no foreshock is observed upstream of the bow shock. Instead, disturbances associated with the quasi-parallel shock are evident far downstream in the yz plane at $x \approx -18.5\,R_E$ and $y < -30\,R_E$ (see the yz plane in Fig. 1d).

Our simulations, consistent with observations, suggest that the size of the magnetosheath is primarily influenced by the dynamic pressure of the solar wind and the angle between the IMF and the Sun–Earth line. When the IMF is aligned with the Sun–Earth line (parallel or antiparallel), the subsolar bow shock gets highly disturbed and mixed into the foreshock, and consequently, the subsolar magnetosheath region gets narrower (i.e. R1 series). Conversely, when the IMF is oriented at an oblique angle to the solar wind, the bow shock forms a well-confined boundary and the subsolar magnetosheath

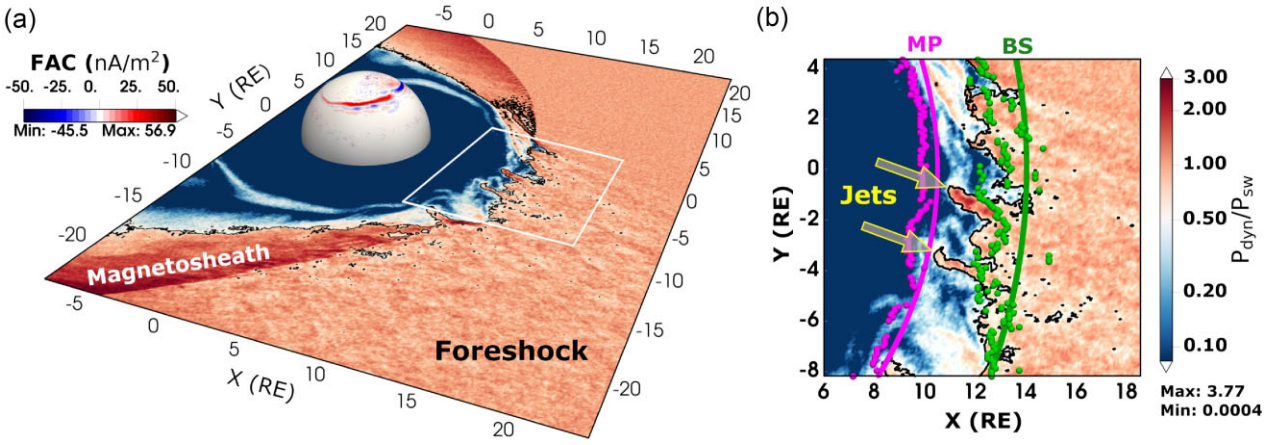

Figure 2. Amitis hybrid simulation results presented in the GSM coordinate system for the R1Y simulation at time $t = 744$ s in the xy (equatorial) plane at $z = 0$. (a) Plasma dynamic pressure in logarithmic scale, normalized to the upstream solar wind dynamic pressure, $P_{sw} = 1.86$ nPa. The sphere centred at the origin of the coordinate system represents the inner boundary of our simulations at 4.7 R_E with a projected intensity of the field-aligned current (FAC). The solid black contour lines show $P_{dyn,x} = 0.5\ P_{sw}$, i.e. the Plaschke criterion for identifying magnetosheath jets, explained in Section 2. (b) A zoomed-in region from the highlighted area with the white rectangle in panel (a) shows the normalized plasma dynamic pressure with two marked magnetosheath jets. The pink and green dots denote, respectively, the magnetopause (MP) and bow shock (BS) boundaries estimated from our simulations. The selection criteria for the MP and BS boundaries are explained in Section 2.4. The solid pink and green lines mark the corresponding boundaries obtained from the empirical model by Chao et al. (2002) for the plasma parameters applied in our simulations and listed in Table 1.

region becomes thicker (i.e. run R2) compared to the quasi-parallel configurations.

Despite noticeable differences in the magnetic field structures presented in various panels in Fig. 1, consistent features are visible in all panels, irrespective of the IMF configuration. These features include the collisionless bow shock, magnetopause, funnel-shaped magnetospheric cusps, and elongated magnetotail. Other fundamental magnetospheric phenomena (e.g. a flux rope over the dayside northern cusp in the magnetosheath at approximately $(+7.5, 0.0, +7.5)\ R_E$, marked with a pink arrow in Fig. 1(a) and Kelvin–Helmholtz-like vortices marked in Figs B1(a) and (e) in Appendix B) have also been observed in our simulations, but analysing them is beyond the scope of this study. In general, Fig. 1 indicates that our simulations provide a reasonable representation of the solar wind plasma interaction with the Earth.

3.2 Magnetosheath jets

Here, we focus on the magnetosheath jets and present their morphology for different IMF configurations. In Fig. 2(a), we present plasma dynamic pressure, P_{dyn}, normalized to the upstream solar wind dynamic pressure, $P_{sw} = 1.86$ nPa, in the equatorial (xy) plane at $z = 0$ for the R1Y simulation run (i.e. a quasi-parallel IMF to the solar wind flow with $B_z = 0$). The solid black contour lines in this figure are obtained from the Plaschke criterion, highlighting $P_{dyn,x} = 0.5\ P_{sw}$. Additionally, we project the field-aligned current density, FAC, onto the inner boundary of our simulation at 4.7 R_E. Different FAC regions are evident in Fig. 2(a), and their structure and current intensity are consistent with previous observations (Milan et al. 2017; Ganushkina, Liemohn & Dubyagin 2018). (See Movies A1 and A2 in Appendix A where we have shown the time evolution of the FACs as well as the plasma flux precipitation into the inner boundary of our simulations).

Our simulation presented in Fig. 2(a) shows that the dynamic pressure is spatially variable in the foreshock region, ranging between 0.05 P_{sw} and 1.65 P_{sw} with the mean value of 0.95 P_{sw} and standard deviation of 0.18 P_{sw}. For visualization purposes, we set the colour bar range for the dynamic pressure between 0.083 P_{sw} and 3.0 P_{sw}, centred at 0.5 P_{sw} (i.e. the Plaschke criterion explained in Section 2.3), while the local minimum and maximum values in our presented simulation results are $4.0 \times 10^{-4}\ P_{sw}$ and 3.77 P_{sw}, respectively. We see from Fig. 2(a) that in some places in the magnetosheath, the dynamic pressure reaches nearly twice the upstream solar wind dynamic pressure, and it gets higher than 3.0 P_{sw} near the magnetospheric flanks. At the subsolar region, a few magnetosheath jets with localized high dynamic pressure are apparent.

For better visualization, Fig. 2(b) provides a closer view of the upstream magnetosheath region, where the presence of high dynamic pressure jets becomes evident. In this figure, similar to Fig. 2(a), the black contour lines highlight $P_{dyn,x} = 0.5\ P_{sw}$, i.e. the Plaschke criterion for identifying magnetosheath jets. Two jets with apparent classical 'cylinder-like' (or finger-like) structures are marked with arrows, displaying significantly higher dynamic pressure compared to their surrounding environment in the magnetosheath ($P_{dyn} \geq 0.5\ P_{sw}$). In addition, the magnetopause and bow shock boundaries estimated from our simulations are shown, respectively, by the pink and green dots. Identifying the subsolar bow shock boundary when the IMF is quasi-parallel to the solar wind flow presents a non-trivial task due to the influence of the foreshock disturbances. The bow shock boundary obtained from our simulations (green dots) stands slightly closer to Earth compared to the bow shock location estimated by Chao et al.'s empirical model for the bow shock (Chao et al. 2002), illustrated by the solid green curve. However, the magnetopause boundary yields a better agreement between our simulations (pink dots) and Chao's empirical model for the magnetopause (solid pink curve).

To further investigate the characteristics of the jets, Fig. 3 shows the detailed electromagnetic and plasma environment obtained from our hybrid simulations, presented in the same format as that shown in Fig. 2(b). We see the plasma density inside jets (especially in the one closer to $y = 0$) is significantly higher compared to the density in the ambient magnetosheath and in the upstream solar wind (Fig. 3a). However, as later shown, this is not necessarily valid for all jets,

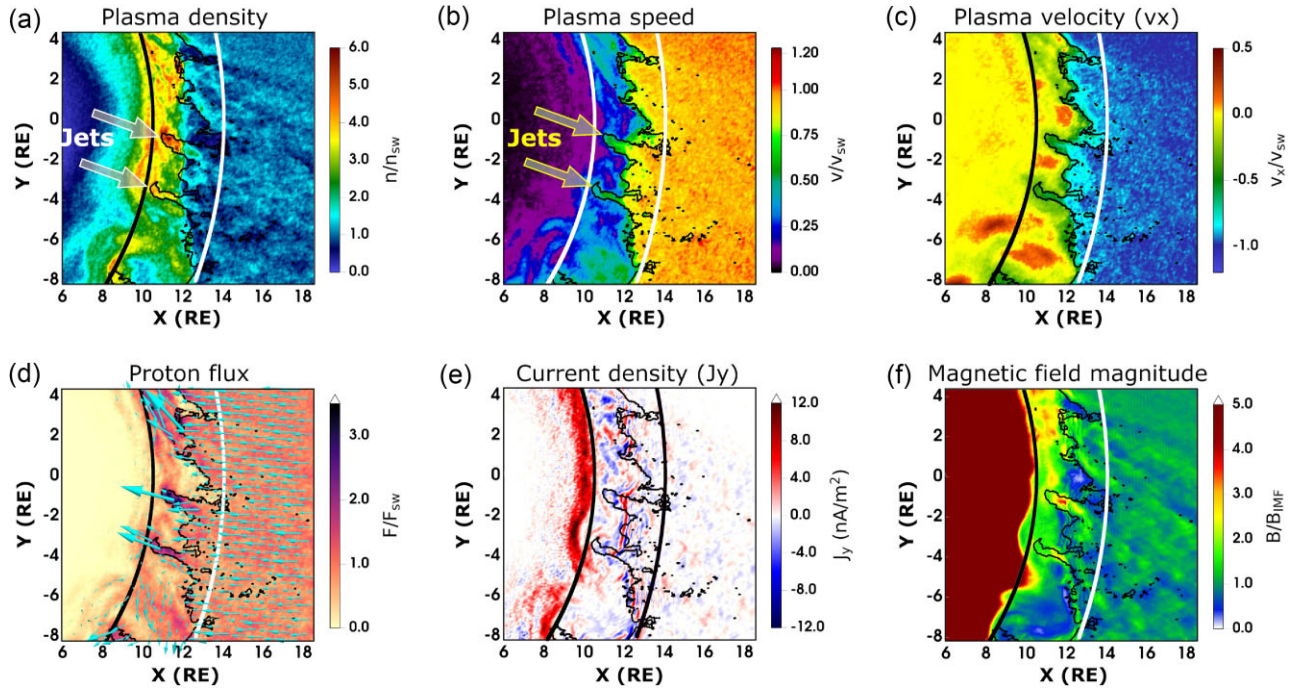

Figure 3. Hybrid simulation results for the R1Y simulation at time $t = 744$ s, presented in the same format as that shown in Fig. 2(b). (a) Proton density normalized to the upstream solar wind density, $n_{sw} = 7\,cm^{-3}$, (b) proton speed normalized to the upstream solar wind speed, $|v_{sw}| = 400\,km\,s^{-1}$, (c) normalized x-component of the proton velocity to the upstream solar wind speed where negative values show the antisunward and positive values show the sunward plasma motion, (d) proton flux normalized to the upstream solar wind flux, $F_{sw} = 2.8 \times 10^{12}\,m^{-2}\,s^{-1}$, and the coloured arrows show the direction and magnitude of the proton flux, (e) the y-component of the electric current density, J_y, and (f) the magnitude of the magnetic field normalized to the strength of the IMF, $B_{IMF} = 5$ nT. The arrows in Figs 3(a) and (b) mark the two magnetosheath jets highlighted in Fig. 2. The inner and outer solid curves in all panels show, respectively, the magnetopause and bow shock boundaries obtained from the empirical model by Chao et al. (2002) for the plasma parameters applied to our simulations, listed in Table 1.

which is consistent with previous observations (Archer & Horbury 2013; Karlsson et al. 2015; Plaschke et al. 2018). The overall speed of the plasma flow in the jets is approximately half of the upstream solar wind speed, and over two times larger than the average plasma speed in the surrounding magnetosheath (Fig. 3b). For example, the averaged plasma speed of the jet closer to $y = 0$ is $\sim 250\,km\,s^{-1}$, which is nearly 65 per cent of the solar wind speed. However, as shown in Fig. 3(c), the surrounding environment of both highlighted jets has a sunward flow motion with v_x exceeding $0.15\,v_{sw}$ (i.e. $\sim 60\,km\,s^{-1}$ moving sunward along the $+x$-axis). Similar sunward flow motion has been previously observed in both spacecraft data and numerical simulations (Shue et al. 2009; Plaschke et al. 2017; Guo et al. 2022).

The proton flux within both jets exceeds 170 per cent of the upstream solar wind flux (Fig. 3d). In addition, at the time snapshot these results are taken, both jets advance towards the magnetopause, shown by arrows in Fig. 3d, extending predominantly in the same direction as the upstream solar wind with some deviations. Their extension in the flow-parallel direction surpasses their dimension in the flow-perpendicular direction, which agrees with previous numerical simulations (Hao et al. 2016a; Palmroth et al. 2018; Guo et al. 2022). Both jets span the distance from the bow shock to the magnetopause, creating a deformation at the magnetopause boundary, evident in the magnetopause current structure shown in Fig. 3(e). Furthermore, the magnetic environment inside the jets shows noticeable changes compared to their surrounding magnetic field in the magnetosheath. For example, the magnetic field strength in the jet located closer to $y = 0$ reaches around 18 nT, i.e. over 3.5 times larger than the strength of the IMF (Fig. 3f). More detailed structures of the plasma flow motion and magnetic field orientation are shown in Fig. B1 in Appendix B. In addition, the time evolution of these jets and their incidence on the magnetopause are shown in Movies A1 and A2 as well as in Fig. B2 in the appendices.

3.3 The third dimension of the jets

Up till now, we have presented two-dimensional (2D) views of the jet properties (Figs 2 and 3) as obtained from the 2D cross-sections of our 3D simulation results, and we have shown that our results are consistent with earlier spacecraft observations (Němeček et al. 1998; Savin et al. 2008; Hietala et al. 2009; Karlsson et al. 2012; Archer & Horbury 2013; Hietala & Plaschke 2013; Plaschke et al. 2013; Gunell et al. 2014; Gutynska et al. 2015; Plaschke et al. 2017; Goncharov et al. 2020; Plaschke et al. 2020; Raptis et al. 2020) and 2D kinetic simulations (Gutynska et al. 2015; Omidi et al. 2016; Hao et al. 2016a; Palmroth et al. 2018; Preisser et al. 2020; Palmroth et al. 2021; Suni et al. 2021; Guo et al. 2022). However, in the following, we will unveil the 3D structure of the jets by including the third dimension and hereby show that the structure and properties of jets are much more complicated than previously thought.

Fig. 4 illustrates the configuration of the magnetosheath jets for the R1Y simulation run in the yz plane (perpendicular to the solar wind flow direction) at different distances from the centre of the Earth. Due to the geometry of these planes, the centre of Fig. 4(a) is closer to the subsolar bow shock, and the centre of Fig. 4(d) is closer to the nose of the magnetopause. The black dots indicate the bow shock boundary obtained from our simulations, and the purple solid contour

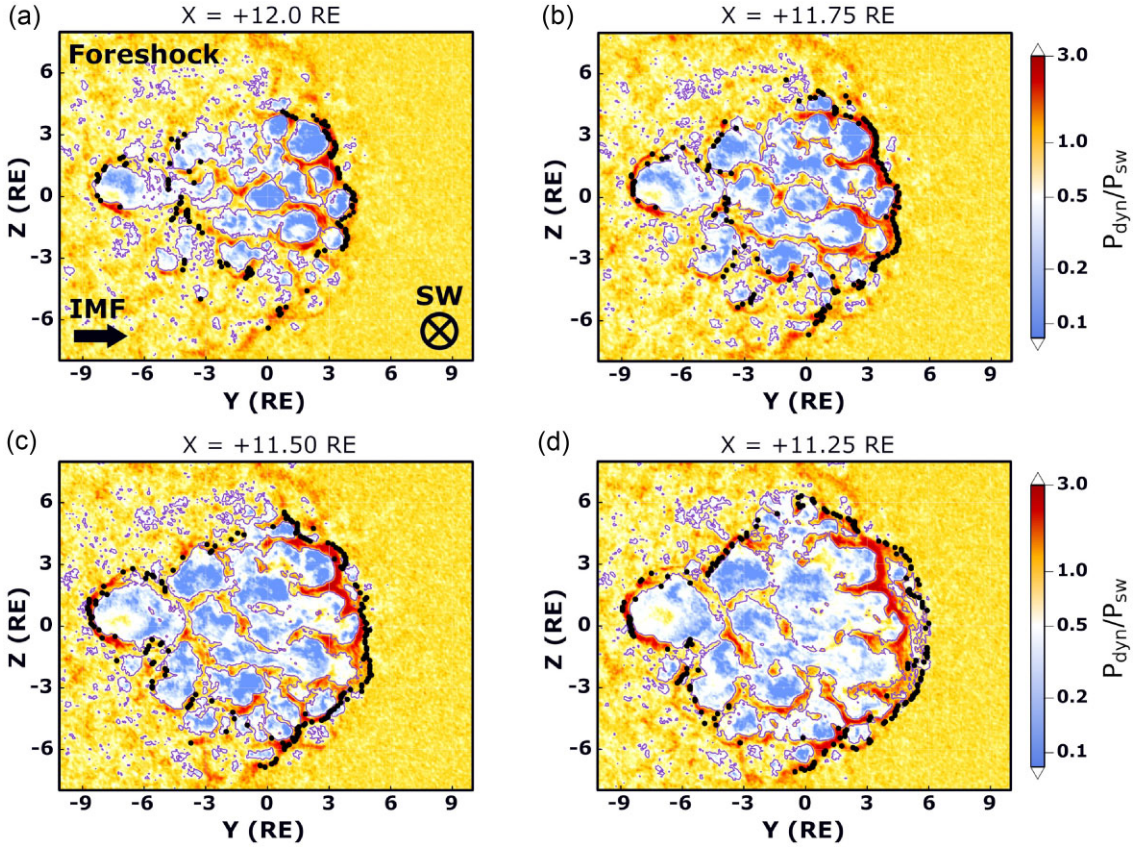

Figure 4. Amitis hybrid simulation results obtained from run R1Y at time $t = 744$ s in the GSM coordinate system, presenting the dynamic pressure normalized to the upstream solar wind dynamic pressure, $P_{sw} = 1.86$ nPa in the yz plane at different distances from the Earth's centre: (a) $x = +12\ R_E$, (b) $x = +11.75\ R_E$, (c) $x = +11.5\ R_E$, and (d) $x = +11.25\ R_E$. The centre of Fig. 4(a) is closer to the subsolar bow shock, and the centre of Fig. 4(d) is closer to the nose of the magnetopause. The black dots indicate the bow shock boundary obtained from our simulations, as explained in Section 2. The magnetosheath is the area surrounded by the bow shock (black dots). The solid purple contour lines highlight $P_{dyn,x} = 0.5\ P_{sw}$ (i.e. the Plaschke criterion for identifying magnetosheath jets). The magnetosheath jets are all the **filamentary structures** with dynamic pressure larger than $0.5\ P_{sw}$ in the magnetosheath (yellow and red in the figure). The Plaschke criterion is valid at the subsolar region within an angle $<30^\circ$ from the Earth–Sun line (Plaschke et al. 2013), which is nearly the entire magnetosheath region presented here. All panels are viewed from the Sun, and therefore the solar wind flows into the planes. The direction of the upstream solar wind flow and the orientation of the undisturbed IMF are the same for all panels and marked by arrows in Fig. 4(a).

lines highlight $P_{dyn,x} = 0.5\ P_{sw}$. As discussed earlier in Section 2, identifying the quasi-parallel shock (black dots scattered at $y < 0$ in all panels in Fig. 4) is a non-trivial task, but the quasi-perpendicular bow shock boundary is well-preserved (black dots at $y > 0$ in all panels in Fig. 4). The magnetosheath is the region surrounded by the bow shock boundary. All the high-dynamic pressure regions ($\geq 0.5\ P_{sw}$) with filamentary structures in the magnetosheath are jets (yellow and red colour regions in the figure).

We present the findings in Fig. 4 using simple 2D cross-sections of our simulations. Alternatively, Fig. B3 in Appendix B presents comparable results on a 3D curved representation of the magnetosheath. In Fig. B3, the normalized dynamic pressure is mapped on a curved structure of the magnetosheath adjacent to the bow shock. Given the complexity of this geometry and the asymmetric nature of the magnetosheath structure, we present our simulation results exclusively on simple 2D flat plans, as shown in Fig. 4. However, the overall structure of the jets presented in Fig. 4 is similar to those shown in Fig. B3.

Contrary to previous hypotheses regarding jet morphology (Archer et al. 2012; Karlsson et al. 2012; Plaschke et al. 2016, 2018; Goncharov et al. 2020; Plaschke et al. 2020; Palmroth et al. 2021; Guo et al. 2022), our 3D kinetic simulations demonstrate that the magnetosheath jets do not exhibit simple geometries like cylinders, spheres, or pancakes. Instead, their structure is exceedingly intricate and interconnected. At closer distances to the bow shock (e.g. Figs 4(a) and (b), the jets appear as interconnected regions. Moving further downstream from the bow shock and getting closer to the magnetopause, the jets are more disconnected as evident in Fig. 4(d). The dynamic pressure inside the jets spans over a wide range from $\sim 0.5\ P_{sw}$ to over $3.0\ P_{sw}$ in the planes shown in Fig. 4.

More detailed characteristics of the jets in the yz plane at $x = +11.5\ R_E$ are shown in Fig. 5. In general, we see from Fig. 5 that the plasma density and velocity of the jets (filamentary structures in the figure) are considerably higher than the surrounding magnetosheath plasma. The time evolution of the jets in the yz plane at $x = +11.5\ R_E$ for the R1Y simulation is shown in the Movie A3 in Appendix A.

The structure of the magnetosheath jets in the yz plane for the southward IMF configuration (run R1S) is illustrated in Fig. 6. In this simulation, both the magnetopause and bow shock are positioned closer to the planet under the southward IMF orientation, primarily due to magnetic reconnection eroding the dayside magnetosphere. This agrees with previous observations and numerical simulations (e.g. Aubry, Russell & Kivelson 1970; Wiltberger, Lopez & Lyon 2003; Le et al. 2016). Consequently, the planes shown in Fig. 6

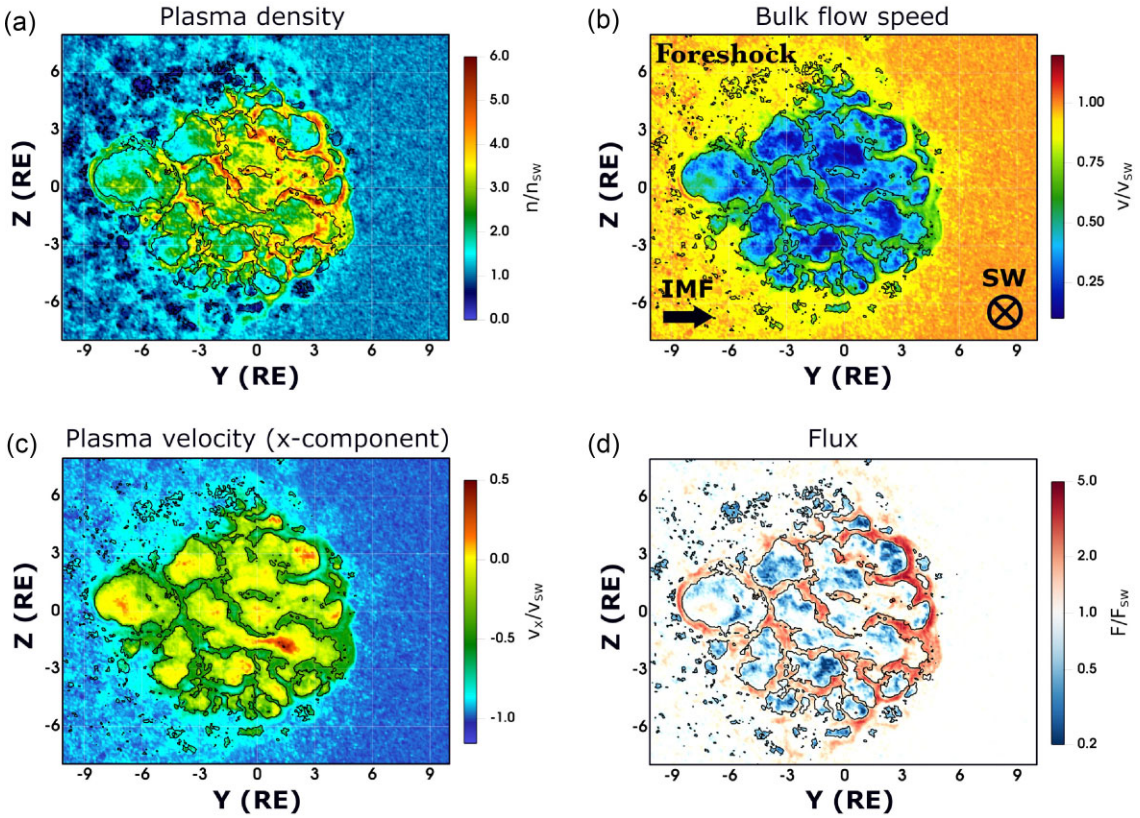

Figure 5. Hybrid simulation results obtained from the R1Y simulation run at time $t = 744$ s in the yz plane at $x = +11.5\ R_E$. The geometry of the cuts is the same as those described in Fig. 4. (a) Proton density normalized to the upstream solar wind density, $n_{sw} = 7\,cm^{-3}$, (b) proton bulk flow speed normalized to the upstream solar wind plasma speed, $v_{sw} = 400\,km\,s^{-1}$, (c) the x-component of the plasma velocity normalized to the upstream solar wind plasma speed, $v_{sw} = 400\,km\,s^{-1}$, and (d) the proton flux normalized to the upstream solar wind flux, $F_{sw} = 2.8 \times 10^{12}\,m^{-2}\,s^{-1}$. The black contour lines show where $P_{dyn,x} = 0.5\ P_{sw}$. The jets are the filamentary structures in the magnetosheath, as described in Fig. 4.

are located closer to Earth compared to those shown in Fig. 4. Similar to the results presented in Fig. 4, the magnetosheath jets exhibit intricate interconnections and form a complex geometry, particularly in proximity to the bow shock (Figs 4(a) and (b)). In contrast to the results shown in Fig. 4, we observe that jets during the southward IMF appear less fragmented and spatially larger and more extended. We expect magnetic reconnection likely plays a role in eroding the field lines at the magnetopause, subsequently altering the dynamics of plasma flow motion in the magnetosheath and affecting the jet's dynamics. However, further investigation and analysis are required to fully understand this phenomenon, which is beyond the scope of this study. In addition, we did not observe any noticeable differences in the average plasma dynamic pressure inside jets during the southward IMF compared to those presented earlier in Fig. 4. A similar conclusion also holds for the northward IMF (see Fig. B4 in Appendix B). To better help with understanding the complex 3D geometry of the jets, we also show the plasma dynamic pressure in the xy plane for the R1S simulation in Fig. B5. However, the overall structure of the jets in the xy plane when the IMF is southward (or northward) is similar to those shown in Fig. 2(a).

Similar to their structure, the evolution of jets is also complex and indeed a 3D problem. Fig. 7 illustrates the angle between the local plasma flow and the upstream solar wind in the yz plane at $x = +11.5\ R_E$, taken at different times from the R1Y simulation. In this figure, the zero degrees (white regions) mean the plasma flow direction is exactly parallel to the upstream solar wind (i.e. along the $-x$-axis). Angles between 0° and 90° indicate an antisunward flow, and angles larger than 90° show a sunward flow. In general, this figure shows how large the plasma flow direction deviates from the undisturbed solar wind flow direction in the shown planes. Similar to Fig. 4, jets are the filamentary structures mainly clustered at the centre of each panel (see Fig. B6 in Appendix B for the time evolution of the dynamic pressure). Fig. 7 indicates the dynamic movement of jets and underscores their lively environment in the yz plane. While the plasma flow motion within jets predominantly follows the solar wind flow direction with nearly 10° to 40° deviation (seen by the light blue regions in Fig. 7), the low dynamic pressure regions encircling the jets in the magnetosheath move predominantly perpendicular to the solar wind and often sunward, which is consistent with previous findings (Shue et al. 2009; Plaschke et al. 2017; Guo et al. 2022).

As shown in Fig. 7, the jets are highly dynamic, intermittently merging into and splitting from each other. For instance, let's consider a half-open loop jet positioned at $(y, z) \approx (+3, +2)\ R_E$, pointed to by an arrow in Fig. 7(a). This jet experiences a phase of closure to another jet after 24 s (Fig. 7b). Subsequently, it reopens after 72 s (Fig. 7(d)) and then progresses towards the equatorial plane (Figs 7(e) and (f)). As shown previously in Fig. 2, and also Fig. B2 in Appendix B, these jets have a third dimension along the x-axis, which makes their geometry not as simple as previously thought.

Consistent with previous observations, our simulations indicate that the low IMF cone angles relative to the solar wind flow direction are favourable for the generation of magnetosheath jets downstream

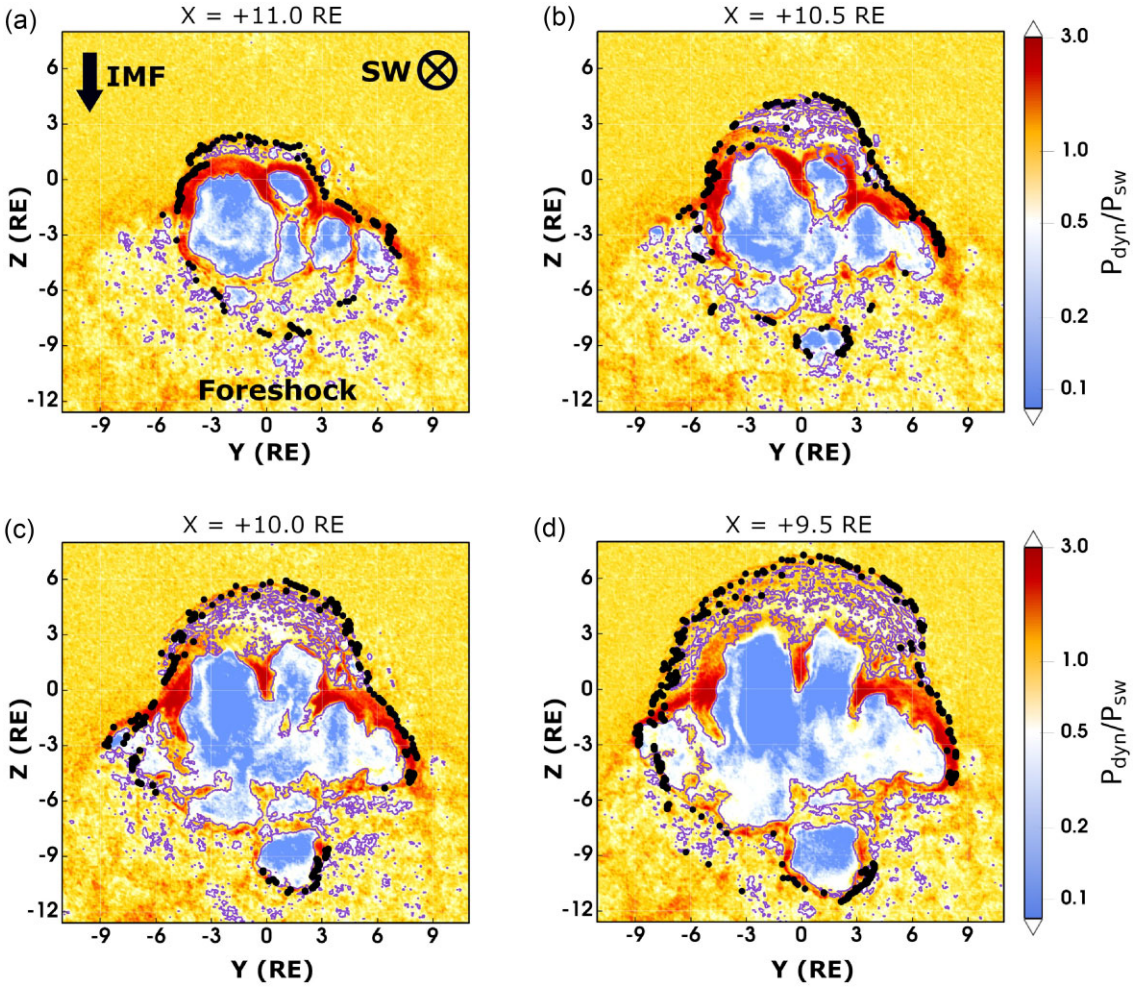

Figure 6. Hybrid simulation results obtained during the southward IMF (run R1S) at time $t = 2244$ s, presenting the dynamic pressure normalized to the upstream solar wind dynamic pressure, $P_{sw} = 1.86$ nPa in the yz plane at different distances from the Earth's centre: (a) $x = +11.0\,R_E$, (b) $x = +10.5\,R_E$, (c) $x = +10.0\,R_E$, and (d) $x = +9.5\,R_E$. The figure format is the same as that shown in Fig. 4. The solid purple contour lines highlight $P_{dyn,x} = 0.5\,P_{sw}$ (i.e. the Plaschke criterion for identifying magnetosheath jets).

of the quasi-parallel shock in the subsolar region (i.e. where the local bow shock normal is quasi-parallel to the IMF) (Archer & Horbury 2013; Plaschke et al. 2013, 2018). In the case of run R2 (i.e. a perpendicular IMF to the solar wind flow), we did not observe jets in the subsolar region. Instead, as shown in Fig. B7 in Appendix B, jet-like structures with various scales manifest downstream of the quasi-perpendicular shock at the magnetosheath flanks, marked with the white arrow in Fig. B7. This finding is in agreement with some of the earlier observations (e.g. Archer & Horbury 2013). Recent studies, however, have suggested that the jets observed downstream of the quasi-perpendicular shock are originally forming at the quasi-parallel shock and later transported downstream of the quasi-perpendicular shock (Raptis et al. 2020; Kajdič et al. 2021). While our preliminary analyses using our simulations (not shown here) do not support this idea, investigating the nature of the jets downstream of quasi-perpendicular shocks requires a separate study.

3.4 Stationary virtual spacecraft observations

To further investigate the characteristics of jets in our model, we placed two stationary virtual observers in our simulations at two distinct locations within the magnetosheath, emulating spacecraft observations. The first observer is positioned downstream near the nose of the bow shock at $(+11.5, 0.0, -1.0)\,R_E$, and the second observer is located in proximity to the magnetopause at $(+10.0, 0.0, +3.5)\,R_E$. The time-series for various parameters derived from our kinetic simulations are shown in Fig. 8. The selected observers are located slightly above and below the equatorial plane. This is because the number of virtual observers distributed throughout our simulation domain is limited, and the one located at $(+11.0, 0.0, 0.0)$, R_E did not observe jets as frequently as those presented in Fig. 8. In addition to these two observers in the magnetosheath, we also placed one virtual observer as a reference point in the solar wind and far away from any terrestrial disturbances. The results from this observer are presented in Fig. B8 in Appendix B.

The first 7.5 min of our simulations are highlighted as the 'development phase' in Fig. 8. This is the minimum time required for the dayside magnetosphere to be developed in our experiments during the nominal solar wind conditions at Earth (see Movies A4 and A5 in Appendix A). Subsequently, the magnetosphere attains a more developed state, and the simulation results reach a steady state. To introduce perturbations into the system, a magnetic transient in the form of a current sheet is applied upstream of our simulations (see Section 2 for more detail and also see time 12:30 in Fig. B8(d) in

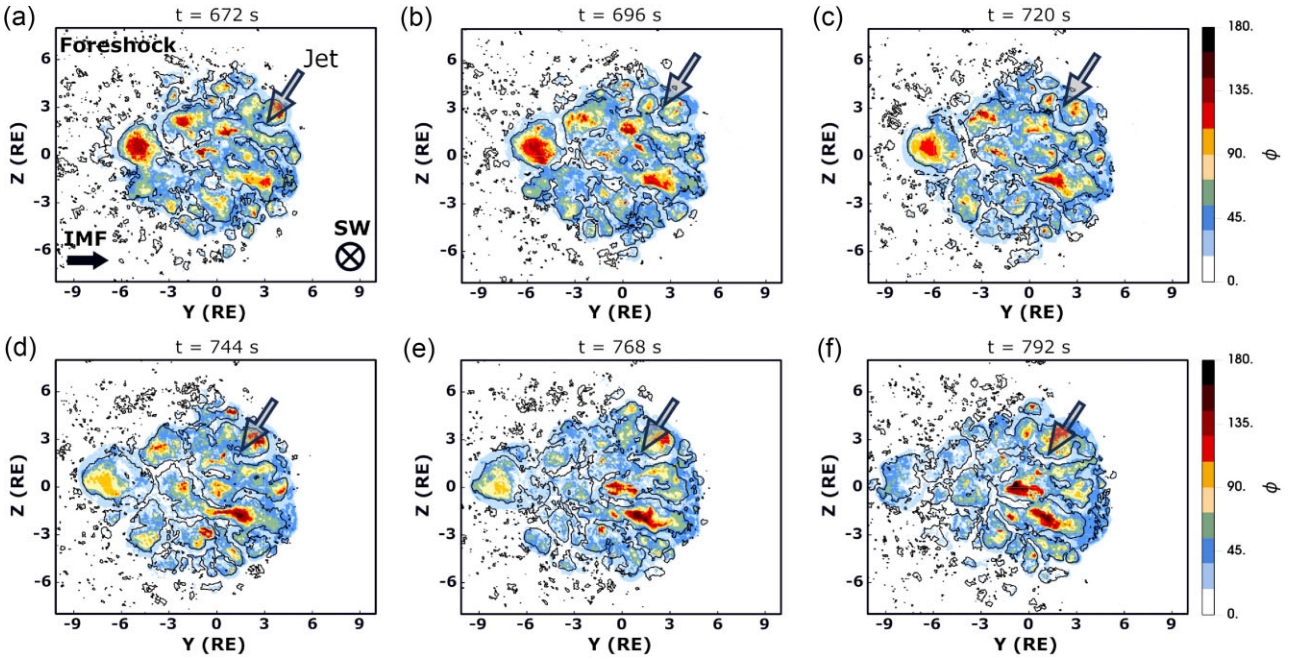

Figure 7. Hybrid simulation results obtained from run R1Y in the *yz* plane at $x = +11.5\ R_E$ at six different simulation times: (a) 672 s, (b) 696 s, (c) 720 s, (d) 744 s, (e) 768 s, and (f) 792 s. The last panel is taken at nearly 400 s prior to the arrival of the southward magnetic transient from the R1S simulation. The background colour illustrates the angle between the localized plasma flow direction and the upstream solar wind flow direction. The zero degree means exactly parallel flow to the solar wind (i.e. along the $-x$-axis). Angles between 0° and 90° are antisunward flow, angles larger than 90° mean sunward flow, and consequently, 180° means perfectly antiparallel to the solar wind flow direction (i.e. along the $+x$-axis). The jets are the filamentary structures, and they have a flow angle of less than ∼40° (light-blue colours). The black arrow in each panel points to one of the magnetosheath jets that gets connected to its neighbouring jets at time 696 s and then gets disconnected again at time 744 s (see the text for more detail). The figure format is the same as that shown in Fig. 4.

Appendix B). This magnetic transient arrives at the first observer at time ∼22:00, and at the second observer around 23:00. These instances of the magnetic transient are highlighted in red in Fig. 8. Prior to the arrival of the magnetic transient and after its passage, the solar wind parameters, and magnetic field configurations remained constant upstream of our simulation domain, indicating a relatively constant environment in terms of solar wind conditions and magnetic field configurations for over 10 min.

In Figs 8(a) and (f), the proton dynamic pressure, $P_{\rm dyn} = mn\boldsymbol{v}^2$, is shown by the solid black line, where m represents the proton mass, n is the plasma density, and $\boldsymbol{v}$ is the plasma flow velocity. The proton dynamic pressure along the solar wind flow direction, denoted as $P_{{\rm dyn},x} = mnv_x^2$, is shown by the solid red line, where v_x is the x-component of the plasma flow velocity. The dashed horizontal line indicates the upstream solar wind dynamic pressure (1.86 nPa) and the dash–dotted horizontal line indicates half of the solar wind dynamic pressure (0.93 nPa). According to the Plaschke criterion, the observed feature with $P_{{\rm dyn},x} \geq 0.93$ nPa are jets. In approximately 30 min after the development phase, we observed many jets passing through both observers in our simulations, some of them are labelled with numbers in the top panels in Fig. 8. The identified jets vary in duration, ranging from a few seconds (e.g. jets #1, #6, and #9) to several minutes (e.g. jets #7, #8, and #10).

Nevertheless, it is essential to recognize that the intricate 3D structure of the jets, as obtained from our simulation results (illustrated in Figs 2–7 and the accompanying supplementary movies in Appendix A), indicates that some of the identified jets in Fig. 8 could be components of the same jet. These components may undergo fragmentation and recombination and appear as seemingly a new jet at later times in the '1D view' presented in Fig. 8. This statement also holds for the previous spacecraft observations of magnetosheath jets.

Comparing Fig. 8(a) with Fig. 8((f), we observe more jets near the bow shock than near the magnetopause, which is consistent with previous observations (Archer & Horbury 2013; Plaschke et al. 2013; Goncharov et al. 2020). In addition, our simulations demonstrate that jets can form during stable IMF configurations, which confirms earlier observations that did not directly relate the formation of the jets to magnetic transients (Archer & Horbury 2013; Plaschke et al. 2013). For example, all labelled jets, except #5, formed during a constant and stable IMF. During the transient event, however, we also observe the passage of a jet through the first observer near the bow shock (i.e. jet #5), which may or may not have been formed by the transient event. Investigating the formation mechanism of the jets is beyond the topic of this research and will be conducted in a separate study.

Noteworthy characteristics of jets can be seen in the second and third rows in Fig. 8. Consistent with previous observations (Archer & Horbury 2013; Plaschke et al. 2018), some jets exhibit a substantial rise in plasma density (e.g. jets #3, #7, and #10), while others do not display significant changes (e.g. jets #2, #4, and #11). However, all the identified jets shown in Fig. 8 demonstrate a substantial increase in their flow velocity. In particular, the x-component of velocity during the passage of nearly all jets, as shown by the red lines in Figs 8(c) and (h), reaches ∼200 km s^{-1} and beyond, which aligns with earlier observations (Archer & Horbury 2013; Plaschke et al. 2013; Gunell et al. 2014; Karlsson et al. 2015). Furthermore, Figs 8(d) and (i) illustrate magnetic field variations, which may be associated with jets, as observed in spacecraft data (Plaschke et al. 2020). However, we collected the simulated magnetic field data at the

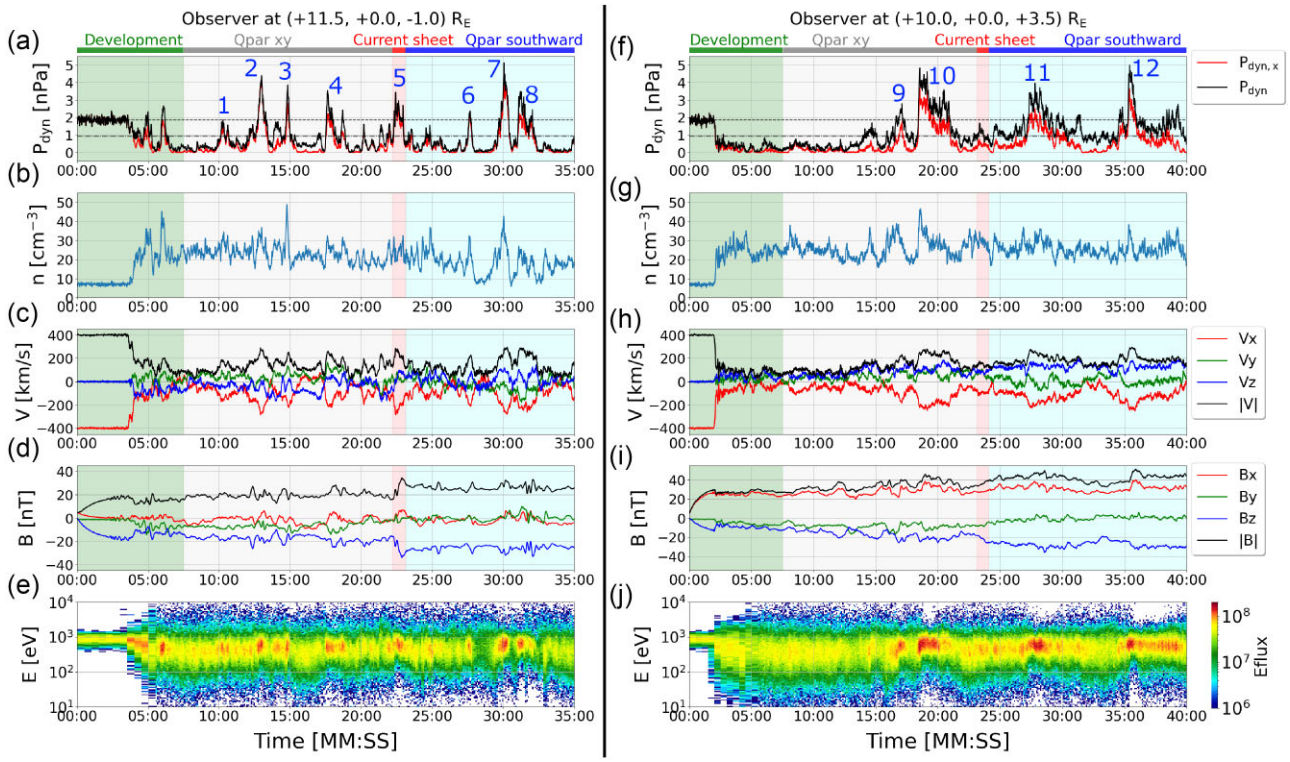

Figure 8. The temporal evolution of various quantities examined at the position of two stationary virtual observers located within the magnetosheath in our hybrid simulations: (a–e) results at the first observer located downstream of the bow shock at (+11.5, 0.0, −1.0) R_E, and (f–j) results at the second observer positioned upstream of the magnetopause at (+10.0, 0.0, +3.5) R_E. (a, f) Proton dynamic pressure, $P_{dyn} = mn_{sw}\boldsymbol{v}^2$, is shown by the solid black line, and the proton dynamic pressure along the solar wind flow direction, denoted as $P_{dyn,x} = mn_{sw}v_x^2$, is shown in red. The dashed horizontal line shows the upstream solar wind dynamic pressure, 1.86 nPa, and the dash–dotted horizontal line marks half of the solar wind dynamic pressure, 0.93 nPa. Several magnetosheath jets, where their $P_{dyn,x} \geq 0.93$ nPa are labelled with numbers. (b, g) Proton density, (c, h) three components of the proton velocity, (d, i) three components of the magnetic field, and (e, j) differential proton energy flux ('Eflux') as a function of energy and time. The initial phase of the magnetosphere development in our model is highlighted in green (i.e. the first 7.5 min). Subsequently, the IMF aligns quasi-parallel to the solar wind flow in the *xy* plane (run R1Y). After approximately 22 min, the current sheet reaches the first observer, and nearly one minute later, it arrives at the second observer. After this, the IMF exhibits a southward orientation for more than 15 min (run R1S). The period encompasses both the R1Y and R1S simulations, during which a current sheet (magnetic transient) traverses the Earth's magnetosphere, highlighted in red. Also, see Fig. B8 in Appendix B for the upstream observer.

location of our virtual observers with a frequency of 0.33 Hz, which is not high enough to pursue wave analysis. The energetic behaviour of jets can also be distinguished in the energy-time spectrogram obtained from our kinetic simulations, as shown in Figs 8(e) and (j). Consistent with previous spacecraft observations (Hietala et al. 2009; Archer et al. 2012; Dmitriev & Suvorova 2012; Archer & Horbury 2013; Plaschke et al. 2013, 2018; Raptis et al. 2022b), the identified jets in our simulations exhibit a higher energy flux and lower plasma heating compared to the classical structure of the magnetosheath plasma without jets.

4 DISCUSSION AND CONCLUSIONS

We present the first 3D, global, hybrid-kinetic plasma interaction between the solar wind plasma and the Earth's magnetosphere using Amitis, a high-performance GPU-based hybrid-kinetic plasma framework (Fatemi et al. 2017). While MHD models have been extensively applied for decades to study the solar wind interaction with the Earth (e.g. Den et al. 2006; Lopez, Merkin & Lyon 2011), the kinetic nature of the interaction, for example, the formation of an extensive foreshock during quasi-parallel IMF configurations cannot be explained by MHD models. Moreover, earlier kinetic simulations applied to this problem are either 2D models (e.g. Omidi et al. 2016; Hao et al. 2016a; Palmroth et al. 2018; Suni et al. 2021; Guo et al. 2022) and/or have scaled down the size of the magnetosphere or the solar wind parameters to reduce the computational costs (e.g. Karimabadi et al. 2014; Omidi et al. 2016; Ng et al. 2021; Omelchenko et al. 2021).

In addition, we present the first 3D structure of magnetosheath jets. Consistent with previous observations and numerical simulations, we show that magnetosheath jets appear during stable IMF configurations, and therefore should not be merely related to transient events in the solar wind. In contrast to earlier findings and analyses, our investigation demonstrates that these jets do not have a simple geometry like a cylinder, sphere, or pancake. Instead, they exhibit a complex 3D and dynamic structure, interlinked in a highly intricate manner. They repeatedly merge into and split from each other, encompassing a broad spectrum of dimensions, and reach the magnetopause over a spatially large area (see Movies A1, A2, and A3 in Appendix A for more details). Quantitative analysis of the size and lifetime of the jets is left for future investigations.

Previous 2D simulations of the magnetosheath jets (Gutynska et al. 2015; Hao et al. 2016a; Palmroth et al. 2018; Preisser et al. 2020; Palmroth et al. 2021; Suni et al. 2021; Guo et al. 2022) may provide a misleading impression of the structure, size, and time-evolution of jets due to their 2D perspective and the lack of the third

dimension. Moreover, 3D simulations without realistic scales for the Earth (Omelchenko et al. 2021) did not yield definitive findings concerning the morphology of jets, primarily due to scaling factors applied to the size of the Earth and/or the strength of the Earth's magnetic dipole. However, our simulations with physical scaling of the Earth's magnetosphere reveal that jets are intricate, dynamic, and indeed, 3D structures.

By analysing the results from our single-point measurements, presented in Fig. 8, we lack additional information about the 3D spatial arrangement of jets. This arrangement resembles spacecraft observations that probe only a small spatial area at once and therefore provide a limited '1D snapshot' view of jets. Consequently, by using the spacecraft data, we cannot definitively determine if the observed jets are numerous individual entities or if they are fewer in number with some being components of an interconnected structure, akin to the examples illustrated in Figs 4–7. This indicates the significance of utilizing 3D kinetic simulations for the magnetosphere to comprehensively explore the morphology of the jets.

Through the exploration of the 3D structure of magnetosheath jets, we can improve our knowledge of the Earth's magnetosphere and its interaction with the solar wind. In addition, recent studies have provided compelling evidence for the formation of magnetosheath jets in planetary magnetospheres beyond our own (Gunell et al. 2023). Therefore, our research not only advances our understanding of magnetosheath jets within the magnetosphere of the Earth but also offers valuable insights into analogous phenomena occurring in other planetary magnetospheres. This can open new windows for comparative planetary research.

ACKNOWLEDGEMENTS

Funding: The authors acknowledge financial support from the Swedish National Space Agency (SNSA) grant 2022–00138. SF also acknowledges financial support from SNSA grant 115/18, the Swedish Research Council (VR) grant 2018–03454, and Nvidia's Academic Hardware Program, grant RTX-A6000. MH & EK also acknowledge financial support from VR grant 2018–03623.

Computation resources: The computations were primarily enabled by the Berzelius resource provided by the Knut and Alice Wallenberg Foundation (KAW) at the National Supercomputer Centre (NSC), Linköping, Sweden, and EuroHPC Regular Access, grant EHPC-REG-2023R03-023. The analyses were partly conducted through computation and data storage resources at the High Performance Computing Center North (HPC2N), Umeä University, Sweden, and partly through infrastructure and hardware grants awarded through 'Kempestiftelserna' and 'medeldyr utrustning' at Umeå University, Sweden. SF acknowledges Prof. Paolo Bientinesi, Mr Åke Sandgren, and Mr Björn Torkelsson at HPC2N for their unconditional support and assistance in providing hardware for running the Amitis code on the Kebnekaise supercomputer.

Author contributions: SF is the developer of the Amitis code, planned and ran all the simulations, performed the analyses, made the figures, and wrote the first draft of the paper. SF and EK developed the post-processing and visualization tools for Amitis simulations in PYTHON. All authors contributed to the discussions and interpretation of the results and improvement of the analyses. They also contributed to editing and improving the text of this manuscript.

DATA AVAILABILITY

The simulation data presented in this manuscript is archived at Zenodo, and publicly accessible via https://doi.org/10.5281/zenodo.8421137.

REFERENCES

Aizawa S. et al., 2021, Planet. Space Sci., 198, 105176
Archer M. O., Horbury T. S., 2013, Ann. Geophys., 31, 319
Archer M. O., Horbury T. S., Eastwood J. P., 2012, J. Geophys. Res.: Space Phys., 117, A5
Aubry M. P., Russell C. T., Kivelson M. G., 1970, J. Geophys. Res., 75, 7018
Bame S. J., Asbridge J. R., Hundhausen A. J., Montgomery M. D., 1970, J. Geophys. Res., 75, 6360
Bochsler P., 2007, A&A Rev., 14, 1
Brain D. et al., 2010, Icarus, 206, 139
Chao J. K., Wu D. J., Lin C.-H., Yang Y.-H., Wang X. Y., Kessel M., Chen S. H., Lepping R. P., 2002, in Cospar colloquia series, 12, p.127
Den M. et al., 2006, Space Weather, 4,6
Dmitriev A. V., Suvorova A. V., 2012, J. Geophys. Res.: Space Phys., 117, A8
Dmitriev A. V., Suvorova A. V., 2015, J. Geophys. Res.: Space Phys., 120, 4423
Eastwood J. P., Lucek E. A., Mazelle C., Meziane K., Narita Y., Pickett J., Treumann R. A., 2005, Space Sci. Rev., 118, 41
Exner W., Simon S., Heyner D., Motschmann U., 2020, J. Geophys. Res.: Space Phys., 125, e2019JA027691
Fatemi S., Holmström M., Futaana Y., 2012, J. Geophys. Res.: Space Phys., 117, A10
Fatemi S., Holmström M., Futaana Y., Barabash S., Lue C., 2013, Geophys. Res. Lett., 40, 17
Fatemi S., Poppe A. R., Delory G. T., Farrell W. M., 2017, J. Phys.: Conf. Ser., 837, 012017
Fatemi S., Poirier N., Holmström M., Lindkvist J., Wieser M., Barabash S., 2018, A&A, 614, A132
Fatemi S., Poppe A. R., Barabash S., 2020, J. Geophys. Res.: Space Phys., 125, e2019JA027706
Fatemi S., Poppe A. R., Vorburger A., Lindkvist J., Hamrin M., 2022, J. Geophys. Res.: Space Phys., 127, e2021JA029863
Fuqua-Haviland H., Poppe A. R., Fatemi S., Delory G. T., de Pater I., 2019, Geophys. Res. Lett., 46, 4151
Ganushkina N. Y., Liemohn M. W., Dubyagin S., 2018, Rev. Geophys., 56, 309
Goncharov O., Gunell H., Hamrin M., Chong S., 2020, J. Geophys. Res.: Space Phys., 125, e2019JA027667
Gunell H. et al., 2012, Phys. Plasmas, 19,7
Gunell H. et al., 2014, Ann. Geophys., 32, 991
Gunell H., Hamrin M., Nesbit-Östman S., Krämer E., Nilsson H., 2023, Sci. Adv., 9, eadg5703
Gunell H., Goetz C., Fatemi S., 2024, A&A, 682, A62
Guo J. et al., 2022, J. Geophys. Res.: Space Phys., 127, e2022JA030477
Gutynska O., Sibeck D. G., Omidi N., 2015, J. Geophys. Res.: Space Phys., 120, 7687
Han D.-S., Nishimura Y., Lyons L. R., Hu H.-Q., Yang H.-G., 2016, Geophys. Res. Lett., 43, 1819
Hao Y., Lembège B., Lu Q., Guo F., 2016a, J. Geophys. Res.: Space Phys., 121, 2080
Hao Y., Lu Q., Gao X., Wang S., 2016b, ApJ, 823, 7
Harned D. S., 1982, J. Comput. Phys., 47, 452
Herčík D., Trávníček P. M., Štverák Š., Hellinger P., 2016, J. Geophys. Res.: Space Phys., 121, 413
Hietala H., Plaschke F., 2013, J. Geophys. Res.: Space Phys., 118, 7237
Hietala H. et al., 2009, Phys. Rev. Lett., 103, 245001
Hietala H. et al., 2012, Ann. Geophys., 30, 33
Hietala H., Phan T. D., Angelopoulos V., Oieroset M., Archer M. O., Karlsson T., Plaschke F., 2018, Geophys. Res. Lett., 45, 1732

Holmström M., 2013, ASP Conf. Ser.: ASTRONUM-2012, 474, Astron. Soc. Pac., San Francisco, p.202
Holmström M., Fatemi S., Futaana Y., Nilsson H., 2012, Earth Planets Space, 64, 237
Jarvinen R., Alho M., Kallio E., Pulkkinen T., 2020, MNRAS, 491, 4147
Kajdič P., Blanco-Cano X., Omidi N., Rojas-Castillo D., Sibeck D. G., Billingham L., 2017, J. Geophys. Res.: Space Phys., 122, 9148
Kajdič P., Raptis S., Blanco-Cano X., Karlsson T., 2021, Geophys. Res. Lett., 48, e2021GL093173
Kallio E., 2005, Geophys. Res. Lett., 32, 6
Kallio E., Janhunen P., 2004, Adv. Space Res., 33, 2176
Karimabadi H. et al., 2014, Phys. Plasmas, 21, 6
Karlsson T., Brenning N., Nilsson H., Trotignon J.-G., Vallières X., Facsko G., 2012, J. Geophys. Res.: Space Phys., 117, A3
Karlsson T., Kullen A., Liljeblad E., Brenning N., Nilsson H., Gunell H., Hamrin M., 2015, J. Geophys. Res.: Space Phys., 120, 7390
Karlsson T. et al., 2018, 36, 655
Kivelson M. G., Russell C. T., 1995, Introduction to space physics. Cambridge Univ. Press, Cambridge, UK
Krämer E., Hamrin M., Gunell H., Karlsson T., Steinvall K., Goncharov O., André M., 2023, J. Geophys. Res.: Space Phys., 128, e2023JA031621
LaMoury A. T., Hietala H., Plaschke F., Vuorinen L., Eastwood J. P., 2021, J. Geophys. Res.: Space Phys., 126, e2021JA029592
Lavraud B., Borovsky J., Ridley A., Pogue E., Thomsen M., Rème H., Fazakerley A., Lucek E., 2007, Geophys. Res. Lett., 34, 14
Le G. et al., 2016, Geophys. Res. Lett., 43, 2396
Le A., Stanier A., Yin L., Wetherton B., Keenan B., Albright B., 2023, Phys. Plasmas, 30, 6
Ledvina S., Ma Y.-J., Kallio E., 2008, Comparative Aeronomy, 29, 143
Liu T. Z., Hietala H., Angelopoulos V., Omelchenko Y., Roytershteyn V., Vainio R., 2019, Geophys. Res. Lett., 46, 7929
Lopez R. E., Merkin V., Lyon J., 2011, Annales Geophysicae, 29, 6, 1129
Milan S. E. et al., 2017, Space Sci. Rev., 206, 547
Müller J. et al., 2012, Icarus, 218, 666
Narita Y., Plaschke F., Vörös Z., 2021, in Maggiolo R., André N., Hasegawa H., Welling D. T., Zhang Y., Paxton L.J., eds, Magnetospheres in the Solar System, p.137
Němeček Z., Šafránková J., Přech L., Sibeck D., Kokubun S., Mukai T., 1998, Geophys. Res. Lett., 25, 1273
Ng J., Chen L.-J., Omelchenko Y., 2021, Phys. Plasmas, 28, 9
Norenius L. et al., 2021, J. Geophys. Res.: Space Phys., 126, e2021JA029115
Omelchenko Y., Chen L.-J., Ng J., 2021, J. Geophys. Res.: Space Phys., 126, e2020JA029035
Omidi N., Berchem J., Sibeck D., Zhang H., 2016, J. Geophys. Res.: Space Phys., 121, 3155
Palmroth M. et al., 2018, Ann. Geophys., 36, 1171
Palmroth M. et al., 2021, Ann. Geophys., 39, 289
Phan T. et al., 2007, Geophys. Res. Lett., 34, 14
Plaschke F., Hietala H., Angelopoulos V., 2013, Ann. Geophys., 31, 1877
Plaschke F., Hietala H., Angelopoulos V., Nakamura R., 2016, J. Geophys. Res.: Space Phys., 121, 3240
Plaschke F. et al., 2017, J. Geophys. Res.: Space Phys., 122, 10
Plaschke F. et al., 2018, Space Sci. Rev., 214, 81, 1
Plaschke F., Hietala H., Vörös Z., 2020, J. Geophys. Res.: Space Phys., 125, e2020JA027962
Poppe A. R., Fatemi S., 2023, Planet. Sci. J., 4, 14
Poppe A. R., Garrick-Bethell I., Fatemi S., 2021, Planet. Sci. J., 2, 60
Preisser L., Blanco-Cano X., Kajdič P., Burgess D., Trotta D., 2020, ApJ, 900, L6
Rakhmanova L., Riazantseva M., Zastenker G., Yermolaev Y., 2023, Front. astron. space sci., 10, 1121230
Raptis S., Karlsson T., Plaschke F., Kullen A., Lindqvist P.-A., 2020, J. Geophys. Res.: Space Phys., 125, e2019JA027754
Raptis S., Karlsson T., Vaivads A., Pollock C., Plaschke F., Johlander A., Trollvik H., Lindqvist P.-A., 2022a, Nat. Commun., 13, 598
Raptis S., Karlsson T., Vaivads A., Lindberg M., Johlander A., Trollvik H., 2022b, Geophys. Res. Lett., 49, e2022GL100678
Rasca A. P., Fatemi S., Farrell W. M., 2022, Planet. Sci. J., 3, 4
Russell C., Hoppe M., 1983, Space Sci. Rev., 34, 155
Savin S. et al., 2008, JETP letters, 87, 593
Savin S. et al., 2012, Ann. Geophys., 30, 1
Shi Z. et al., 2022, Geophys. Res. Lett., 49, e2022GL098415
Shue J.-H., Chao J.-K., Song P., McFadden J., Suvorova A., Angelopoulos V., Glassmeier K., Plaschke F., 2009, Geophys. Res. Lett., 36, 18
Suni J. et al., 2021, Geophys. Res. Lett., 48, e2021GL095655
Tóth G., Chen Y., Gombosi T. I., Cassak P., Markidis S., Peng I. B., 2017, J. Geophys. Res.: Space Physics, 122, 10
Voitcu G., Echim M., 2018, ANGEO, 36, 6, p.1521
Vuorinen L., Hietala H., Plaschke F., 2019, 37, 689
Walt M., 1994, Camb. Atmos. Space Sci. Ser., 10
Wang B., Nishimura Y., Hietala H., Lyons L., Angelopoulos V., Plaschke F., Ebihara Y., Weatherwax A., 2018, J. Geophys. Res.: Space Phys., 123, 4879
Wang B., Nishimura Y., Hietala H., Angelopoulos V., 2022, Geophys. Res. Lett., 49, e2022GL099768
Wang X.-D., Fatemi S., Nilsson H., Futaana Y., Holmström M., Barabash S., 2023, MNRAS, 521, 3597
Wiltberger M., Lopez R. E., Lyon J. G., 2003, J. Geophys. Res.: Space Phys., 108, A6
Zhou Y., Raptis S., Wang S., Shen C., Ren N., Ma L., 2024, Nat. Commun., 15, 4

SUPPORTING INFORMATION

Supplementary data are available at *MNRAS* online.
Please note: Oxford University Press is not responsible for the content or functionality of any supporting materials supplied by the authors. Any queries (other than missing material) should be directed to the corresponding author for the article.

APPENDIX A: SUPPLEMENTARY MOVIES

Five movies provide supporting information to the main text and figures in our manuscript.

Movie A1.

Amitis hybrid-kinetic simulation results presented in the GSM coordinate system for the R1Y simulation from time 640 s (i.e. 10:40) to 1200 s (i.e. 20:00) in the *xy* (equatorial) plane at $z = 0$. The background colour, similar to Fig. 2 in the main text, shows plasma dynamic pressure in logarithmic scale, normalized to the upstream solar wind dynamic pressure, $P_{sw} = 1.86$ nPa. The sphere centred at the origin of the coordinate system represents the inner boundary of our simulation at 4.7 R_E with a projected plasma flux precipitating into the inner boundary, normalized to the solar wind flux $F_{sw} = 2.8 \times 10^{12}\,m^{-2}\,s^{-1}$. The solid black contour lines show $P_{dyn,x} = 0.5\,P_{sw}$, i.e. the Plaschke criterion for identifying magnetosheath jets, explained in the Model and Methods section in the main text.

Movie A2.

Similar to Movie A1, but showing different quantities. In this movie, the background colour shown in the *xy* plan illustrates the *y*-component of the electric current density, J_y in the units of the nA/m^2. The sphere shows the inner boundary of our simulation at 4.7 R_E with projected FAC at the boundary.

Movie A3.

Amitis hybrid simulation results obtained from run R1Y from time 640 s (i.e. 10:40) to 1200 s (i.e. 20:00) in the GSM coordinate system, presenting the dynamic pressure normalized to the upstream solar wind dynamic pressure, $P_{sw} = 1.86$ nPa in the *yz* plane at $x = +11.5\ R_E$, similar to the time snapshot shown in Fig. 4(c) in the main

text. The geometry of the plan is similar to those shown in Fig. 4 in the main text.

Movie A4.

Amitis hybrid-kinetic simulation results show the global structure of the solar wind plasma interaction with the Earth. The background colour shows the magnitude of the magnetic field in logarithmic scale in (left) the xy plane at $z = 0$ and (right) the xz plane at $y = 0$, both presented in the GSM coordinate system. The presented planes are perpendicular to each other, showing the 3D structure of the magnetic fields. The solar wind flows along the $-x$-axis (from right to left), shown by the yellow arrows. The orientation of the IMF is also shown by the white arrow on each plane. This movie shows in total 40 min of real-time solar wind interaction with Earth, covering the R1Y and R1S simulations. From time 00:00 to 14:20, the IMF is on the xy plane with $B_z = 0$ (i.e. run R1Y). At time 14:20, a current sheet arrives at $x = +40\ R_E$, where the IMF orientation changes southward without changing its initial magnitude (i.e. run R1S). After $\approx$7 min, the current sheet reaches the dayside magnetosphere. Before the arrival of the current sheet, the ion foreshock region is visible upstream of the bow shock on the xy plane. During the passage of the current sheet, the entire system including the foreshock, bow shock, and the magnetosphere, responds to the changes in the IMF orientation. After that, the foreshock region is mainly visible in the xz plane. Since the magnitude of the IMF and solar wind plasma parameters remain unchanged during the entire simulation, no signature of the current sheet is evident in this movie. The IMF magnitude is 5 nT, marked as $|B_{IMF}|$ on the colour bar.

Movie A5.

Amitis hybrid-kinetic simulation results show the global structure of the solar wind plasma interaction with Earth. The background colour shows the plasma density in logarithmic scale in (left) the xy plane at $z = 0$ and (right) the xz plane at $y = 0$, both presented in the GSM coordinate system. The geometry of the planes is similar to those presented in Movie A4. The solar wind plasma density is $7\,cm^{-3}$, marked as n_{sw} on the colour bar.

APPENDIX B: SUPPLEMENTARY FIGURES

Here, we present figures that provide supporting information to the main text and figures in our manuscript.

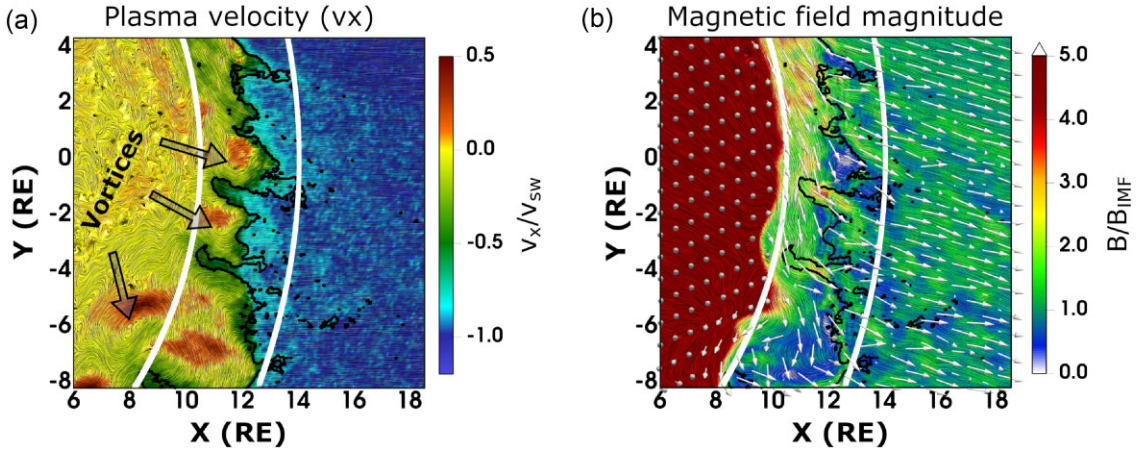

Figure B1. Hybrid simulation results in the *xy* (equatorial) plane from a zoomed-in region to the white rectangle in Fig. 2(a) in the main text. The geometry of the cuts is the same as those described in Fig. 2. Both panels here were previously shown in Fig. 3. Here, we have added more details to them that could not become apparent in Fig. 3. (a) Similar to Fig. 3(c). The background colour shows the x-component of the solar wind velocity, v_x, normalized to the upstream solar wind speed, $v_{sw} = 400\,\mathrm{km\,s^{-1}}$. The streamlines show the direction of the plasma flow motion. Both jets have a forward velocity component towards the magnetopause, and a few Kelvin–Helmholtz-like vortices are visible in this panel, marked by arrows. (b) Similar to Fig. 3(f). The background colour shows the magnitude of the magnetic field normalized to the strength of the IMF, $B_{IMF} = 5\,\mathrm{nT}$. The background streamlines together with arrows show the direction of the magnetic field. Inside the magnetosphere ($x \lesssim 9\,R_E$), the magnetic field lines primarily point northward (outward in the plane shown), and therefore only the arrowheads are visible.

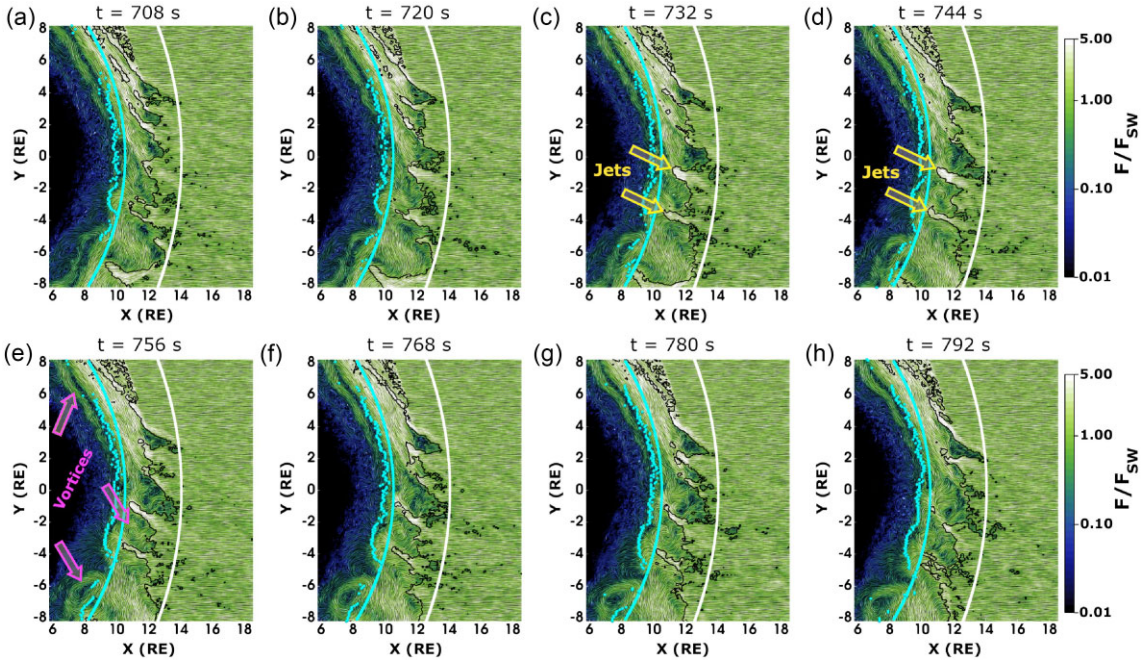

Figure B2. Time evolution of the magnetosheath jets in the *xy* plane at $z = 0$ obtained from our hybrid plasma model for the R1Y simulation setup. Background colour is the normalized proton flux on a logarithmic scale. The streamlines show the direction of the plasma flow. The solid contour lines mark $P_{dyn} = 0.5\,P_{SW}$. Several jets can be seen at different times, and, for example, two of them are marked by yellow arrows in panels c and d. In addition, a few Kelvin–Helmholtz-like vortices are apparent in several panels, and three of them are marked by pink arrows in panel e. The cyan dots denote the magnetopause boundary estimated from our simulations. The solid cyan and white lines, respectively, mark the magnetopause and bow shock boundaries from the empirical model by Chao et al. (2002). The geometry of the planes is similar to those presented in Fig. 3 in the main text.

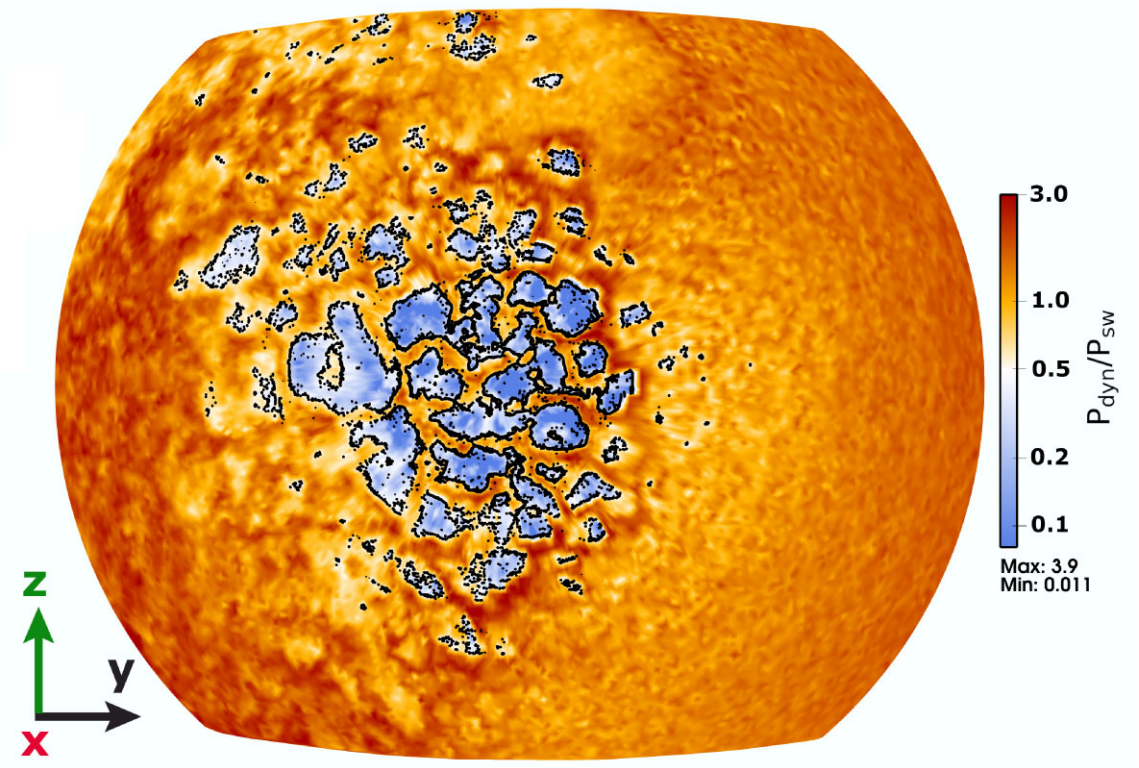

Figure B3. Amitis hybrid simulation results obtained from run R1Y at time $t = 744$ s in the GSM coordinate system, presenting the dynamic pressure normalized to the upstream solar wind dynamic pressure, $P_{sw} = 1.86$ nPa mapped on a 3D curved structure in the magnetosheath adjacent to the bow shock. The solid black contour lines highlight $P_{dyn,x} = 0.5\ P_{sw}$ (i.e. the Plaschke criterion for identifying magnetosheath jets). Given the complexity of this geometry and the asymmetric nature of the magnetosheath structure, we present our simulation results exclusively on simple 2D flat plans, as shown in Figs 4–7 in the main text. This figure here is added to demonstrate that the structure of the magnetosheath presented in the main text is not associated with the geometry of the 2D slices. Indeed, the jet structures shown in Figs 4–7 are similar to those mapped on a 3D curved plane shown here.

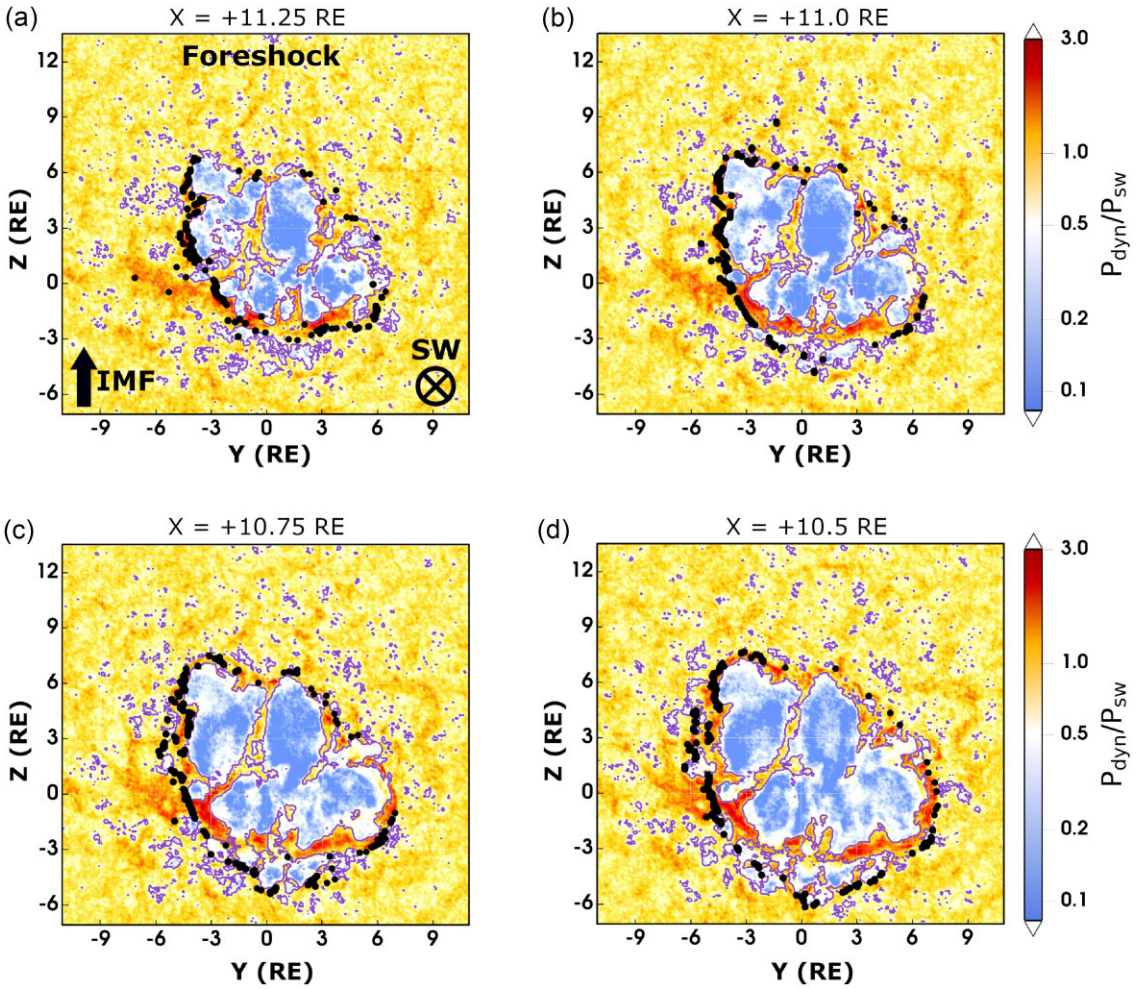

Figure B4. Hybrid simulation results obtained during the northward IMF (run R1N) at time $t = 3060$ s, presenting the dynamic pressure normalized to the upstream solar wind dynamic pressure in the yz plane at different distances from the Earth's centre: (a) $x = +11.25\ R_E$, (b) $x = +11.0\ R_E$, (c) $x = +10.75\ R_E$, and (d) $x = +10.5\ R_E$. The figure format is the same as that shown in Figs 4 and 6 in the main text.

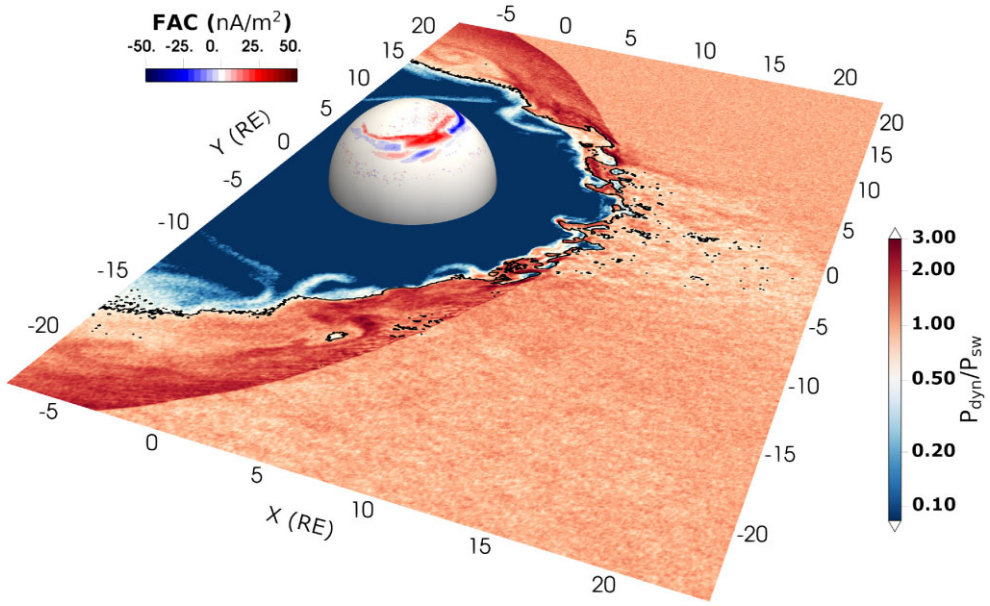

Figure B5. Plasma dynamic pressure in logarithmic scale, normalized to the upstream solar wind dynamic pressure, $P_{sw} = 1.86$ nPa for the R1S simulation in the *xy* (equatorial) plane at $z = 0$. The sphere centred at the origin of the coordinate system represents the inner boundary of our simulations at 4.7 R_E with a projected intensity of the FAC. The figure format is similar to that shown in Fig. 2b in the main text.

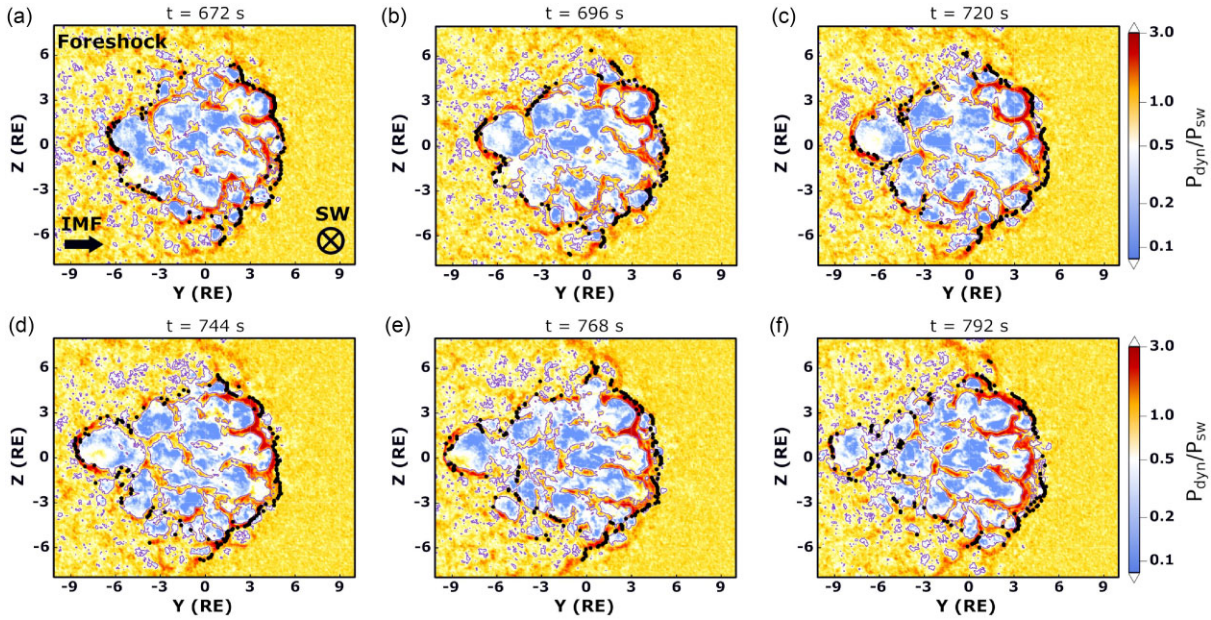

Figure B6. Hybrid simulation results obtained from run R1Y in the yz plane at $x = +11.5$ R_E at six different simulation times: (a) 672 s, (b) 696 s, (c) 720 s, (d) 744 s, (e) 768 s, and (f) 792 s. The background colour illustrates the normalized dynamic pressure. The solid black contour lines highlight $P_{dyn,x} = 0.5$ P_{sw} (i.e. the Plaschke criterion for identifying magnetosheath jets), and the black dots indicate the bow shock boundary obtained from our simulations, explained in the Materials and Methods section. The magnetosheath is the region surrounded by the bow shock boundary, and the jets are the filamentary structures with dynamic pressure ≥ 0.5 P_{sw} in the magnetosheath. The figure format is the same as that shown in Fig. 7 in the main text.

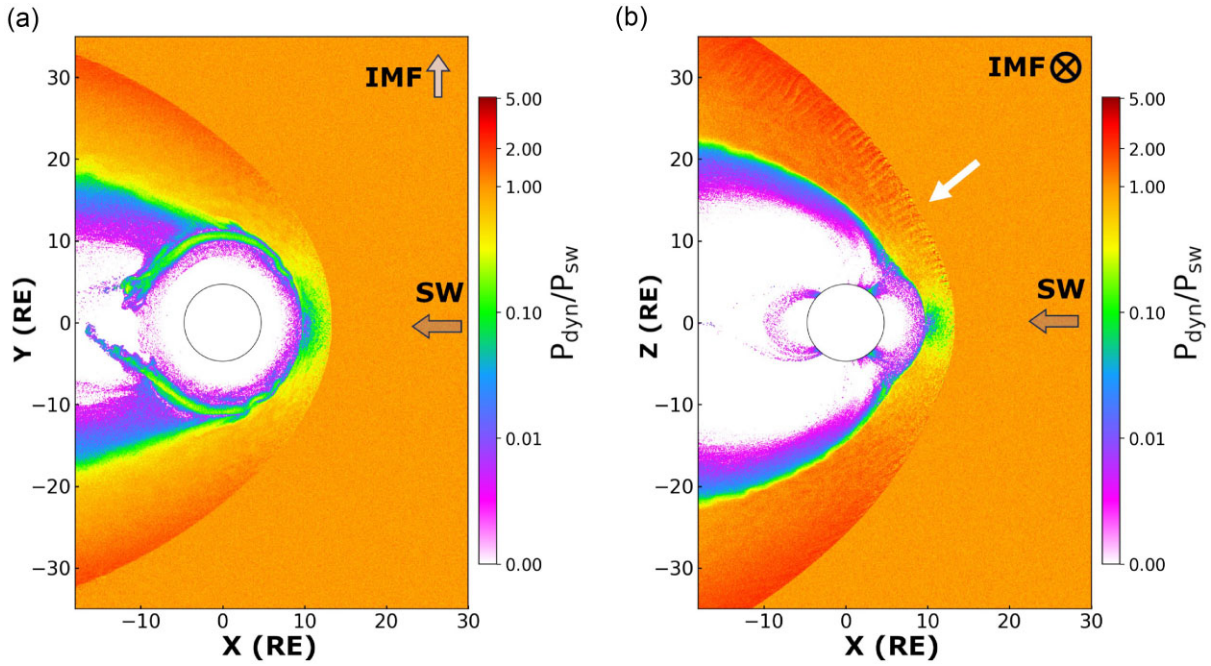

Figure B7. Hybrid simulation results when the IMF is perpendicular to the solar wind (run R2), obtained at time $t = 900$ s, presenting the dynamic pressure normalized to the upstream solar wind dynamic pressure, $P_{sw} = 1.86$ nPa in the (a) xy plane at $z = 0$ and in the (b) xz plane at $y = 0$. The solar wind and IMF orientations at different planes are shown by grey arrows. In panel b, the solar wind convective electric field, $\mathbf{E} = -\mathbf{v} \times \mathbf{B}$, is pointing upward along the $+z$-axis. The white arrow in panel b points to the quasi-perpendicular shock where many small irregular filamentary features, somewhat similar to the magnetosheath jets, are evident downstream of the quasi-perpendicular shock at the +E hemisphere of the magnetosphere. Identifying the nature and characteristics of these filamentary structures are outside the scope of the current study, and will be investigated in a separate research.

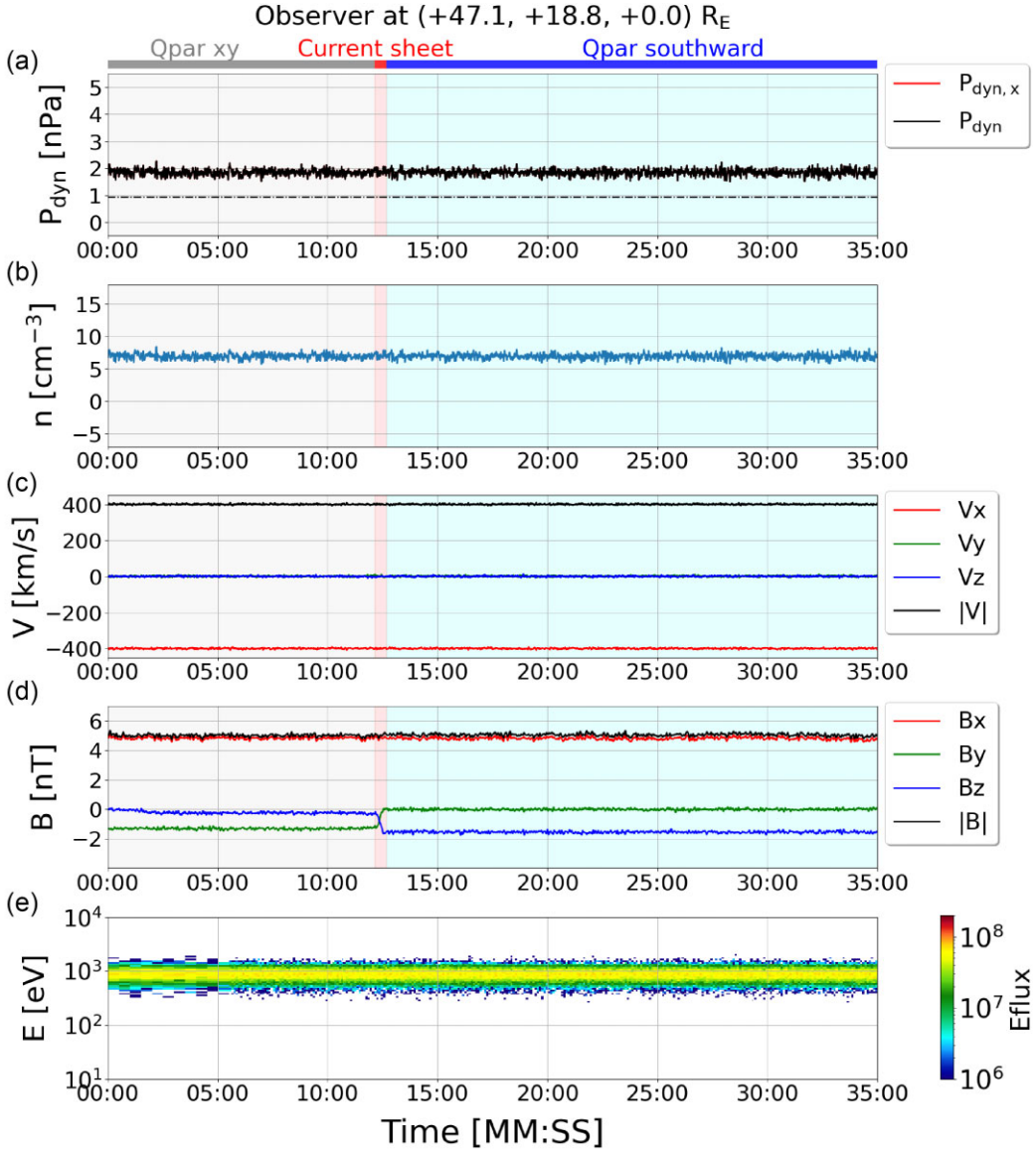

Figure B8. The temporal evolution of (a) plasma dynamic pressure, (b) proton density, (c) proton velocity, (d) magnetic field, and (e) differential proton flux, examined at the position of a stationary virtual observer located in the solar wind and far away from any magnetospheric and foreshock disturbances at (+47.1, +18.8, 0.0) R_E. The magnetic transient (current sheet) arrives at the observer at time ≈12:30, highlighted in red. The description of different panels is the same as that shown in Fig. 8 in the main text. We intentionally did not place the observer only along the *x*-axis to ensure the terrestrial disturbances do not reach the observer during the magnetic transients.

This paper has been typeset from a TEX/LATEX file prepared by the author.